RSC Advances

PAPER

View Article Online
View Journal | View Issue

Cite this: *RSC Adv.*, 2026, **16**, 6164

Investigating the adsorption performance of CO_2, SO_2, NH_3 and CH_4 molecules on $Sb_3(TM)O_6$ (TM = Sc, Ti, V, Cr, Mn, Fe, Ni, and Co) clusters for gas-sensing applications

Nimra Zaib Raza,[a] Abdul Majid, *[a] Sajjad Haider[b] and Kamran Alam[c]

Received 26th October 2025
Accepted 28th December 2025

DOI: 10.1039/d5ra08222f

rsc.li/rsc-advances

Inorganic molecular clusters (IMCs) belong to a trending class of materials with unique structures and properties. Due to having a gap among the cages, they attract the attention of many researchers. This study is carried out in order to investigate the mechanism of adsorption of CO_2, SO_2, NH_3 and CH_4 gases on $Sb_3(TM)O_6$ (where TM is Sc, Ti, V, Cr, Mn, Fe, Ni, and Co) molecular clusters for gas-sensing applications. The structural and electronic properties, along with chemical stability, are determined through density functional theory (DFT) and molecular dynamics (MD) simulations. The adsorption energy of $Sb_3(TM)O_6$ for the CO_2, SO_2, NH_3 and CH_4 gases is calculated. The properties and charge analysis of fully loaded clusters are studied through quantum topology of atoms in molecule (QTAIM) and charge-transfer integrals.

1. Introduction

The increasing amount of atmospheric pollutants is posing huge threats to human health, industrial safety and environmental sustainability. The detection and monitoring of harmful gases, like carbon dioxide (CO_2), nitrogen dioxide (NO_2), methane (CH_4), and ammonia (NH_3), are very important for industrial safety, protection and health.[1] Inorganic molecular clusters (IMCs) belong to a unique category of materials and are distinct from traditional materials. These IMCs are a source of interest for many researchers as they have structural gaps in between them. The detailed structure–property relationship of these IMCs has been reported on the basis of QTAIM (quantum topology of atoms in molecule), NBO (natural bond orbitals) and ETS-NOCV (extended transition state along with natural orbitals chemical valence).[2,3] Their electronic and transport properties have also been investigated in detail.[4] The rapidly growing population demands more energy sources to meet the energy requirements of daily life.[5–7] Although fossil fuels play a vital role in the energy industry, their combustion contributes a lot to air pollution by varying the air composition and emitting harmful gases.[8,9] Internal combustion engine vehicles (ICEVs), as a significant extension of automobiles and industrialization, pose severe threats to human health and the environment by polluting the atmosphere.[10–13] With the rapid economic development and the limitless advancements in modern industry, the world is facing a serious environmental crisis. Humans and the environment are exposed to the severe hazards of toxic and flammable gases.[14,15]

According to the World Health Organization, a new epidemic may erupt due to fluctuations in relative humidity (RH) and temperature.[16] Due to harsh atmospheric conditions, the world is facing a surge in severe respiratory ailments, and the amplification of air pollution, driven by climate change, is responsible for 11.8% (6.7 million) of all global casualties.[17,18] One of the basic causes of these environmental crises and health issues is the emission of toxic gases, including greenhouse gases, methane (CH_4), ammonia (NH_3), carbon dioxide (CO_2) and sulfur dioxide (SO_2). Due to these emissions, the world is experiencing limited access to clean air. During the past few years, the concentration of these gases in the atmosphere has increased tremendously.[19] Thus, for public health safety and industry applications, effective gas sensing, particularly for toxic gases, is crucial. Sensing technology has become the most important supporting column of information technology (IT), which presents lots of opportunities for scientists. It has become the center of focus in the research field as the world is moving forward in the era of Artificial Intelligence (AI) and Internet of Things (IOT). Gas-sensing devices are receiving great attention due to their beneficial applications, and they also deliver tremendous results. The development of novel materials to upgrade the current gas-sensing technologies is at the heart of current research efforts.[20,21]

[a]*Department of Physics, University of Gujrat, Gujrat 50700, Pakistan. E-mail: abdulmajid40@yahoo.com*

[b]*Chemical Engineering Department, College of Engineering, King Saud University, P. O. Box 800, Riyadh 11421, Saudi Arabia*

[c]*Department of Chemical Engineering Materials Environment, Sapienza University of Rome, Italy*

Table 1 Adsorption energies of different reported molecular clusters

Sr. no	Clusters	Gases	Adsorption energy (eV)	Reference
1	Pb_4Au_4	CO	−1.062	47
2	Pb_6Au_6		−1.439	47
3	Pb_8Au_8		−1.325	47
4	N/B_9	NO_2	−11.64	46
5	N/B_9	CO	−12.08	46
6	N/B_9	NH_3	−7.22	46
7	N/B_9	CO_2	−16.57	46
8	MgONTs	H_2O	−0.967	48
9	MgONTs	NH_3	−0.932	48
10	MgONTs	CO	−0.35 to −0.16 eV	48
11	MgONTs	NO	−0.28 to −0.13 eV	48

It has become the need of the time to establish reliable gas-detecting devices. Gas-sensing devices also have potential applications in the field of medicine for identifying several diseases, producing wearable electronics and ensuring food safety.[22–24] The value of the global gas-sensor market has grown from US$3.4 billion to US$5.6 billion over the last decade, which highlights the surge in research on gas-sensing technologies.[25] On the nanoscale, the development of new materials provides the foundation for the advancement of gas-sensing technologies.[26,27] On the basis of increased requirements of improvement in synthesis strategies of high-quality materials, this field has earned significant research attention in the recent past.[28–32]

Nanostructured materials, on account of their selectivity, sensitivity, quick responses, power and energy efficiency, have been considered suitable for use in next-generation gas sensors.[33,34] Gas sensors hold a significant place among newly developed advanced devices as they promise environmental safety by providing real-time information about the concentration of toxic gases in the atmosphere and detecting natural gas emissions.[30,35] These circumstances motivate scientists to advance the field of gas sensing, prioritizing the downscaling of materials to 0D structures.[36–40] The interactions between materials and adsorbate molecules are of great significance for examining their gas-sensing abilities.

Recently, both academia and industry have been paying increasing attention to gas sensing due to its waste-treatment and other applications in intelligence systems. These applications include the detection of methane in mines, medical applications, environmental research, vehicle-pollutant detection, and indoor pollutant monitoring. Gas sensing using 0D materials, *i.e.*, nanoparticles, atomic clusters, quantum dots and bulk-like materials, exhibits exceptional advantages. These materials offer quantum confinement effects, changing morphological characteristics and offering high surface-to-volume ratios, making them suitable for developing gas-sensing technology with enhanced sensitivity, response, time stability and selectivity.[41] Recently, the adsorption properties of Pb_nAu_n nano-clusters have been examined for the removal of toxic gases, such as CO and NO. The calculated adsorption energies using GGA-PW91 ranged from −1.152 eV to −0.995 eV for Pb_nAu_n–NO and −1.062 to −1.443 eV for Pb_nAu_n–CO. The clusters with n values of 2, 4, and 6 are considered more effective due to their pronounced response and chemical stability during gas interactions.[42–45] The adsorption study of gases on the N/B_9-QD structure revealed that the adsorption energy of N/B_9-QDs is much higher than that of simple-structure B_9-QDs. The findings revealed relatively high adsorption energy values of −16.57, −12.08, −11.64 and −7.22 eV for CO_2, CO, NO_2, and NH_3, respectively.[46]

A comprehensive literature review of 0D clusters with their adsorption energies is given in Table 1. The current study reports a comprehensive analysis of the Sb_4O_6 cluster, which is nearly inert on account of its bonding characteristics. In order to tailor its properties for sensing different gases, its structure is modified through the substitution of Sb atoms with transition-metal atoms. This study systematically investigates eight modified $Sb_3(TM)O_6$ structures (where TM is Sc, Ti, V, Cr, Mn, Fe, Ni, Co) by calculating their structural and electronic properties, along with their thermal stability. The adsorption mechanisms of CO_2, SO_2, NH_3, and CH_4 gas molecules on the clusters are studied. Charge analysis is performed by the charge-transfer integral analysis, and the stability of the fully loaded structure is determined by molecular dynamics experiments.

2. Computational details

The entire work is carried out using the Amsterdam Density Functional (ADF)-BAND package, which employs the linear combination of atomic orbitals approach.[49] The PBE functional with a TZP basis set and the ZORA scalar relativistic treatment, which is widely used for transition-metal-oxide clusters, was used for all computations. We employed the hybrid functional for comparison with sample adsorption implementations in order to verify the validity of this level of theory. PBE/TZP/ZORA was found to offer a reliable and suitable framework for this investigation based on this validation and the substantially lower computational cost required to produce the entire dataset. The convergence of the force and energy gradient criteria was set below 0.027 eV $Å^{-1}$ and 0.00027 eV, respectively, during the SCF cycles. The computations were conducted to determine the adsorption energy of the $Sb_3(TM)O_6$ (where TM is Sc, Ti, V, Cr, Mn, Fe, Ni, Co) molecular clusters. The electronic properties of the $Sb_3(TM)O_6$ (where TM is Sc, Ti, V, Cr, Mn, Fe, Ni, Co) molecular clusters for the frontier molecular orbital, DOS, and PDOS were determined. The chemical potential (μ) of the clusters was determined using eqn (1).[50]

$$\mu = -\frac{(E_{HOMO} + E_{LUMO})}{2} \quad (1)$$

The energies of the higher occupied molecular orbital (HOMO) and lower unoccupied molecular orbital (LUMO) orbitals were computed. The energy gap between the HOMO and LUMO, denoted as $\Delta E = E_{HOMO} - E_{LUMO}$, is useful for defining the electrical conductivity.[50] The values of the electrical conductivity ΔE, chemical hardness (η) and softness (S), and electrophilicity (ω) are derived using eqn (2)–(4).[51,52]

$$\eta = \frac{(-E_{HOMO} + E_{LUMO})}{2} \quad (2)$$

$$S = \frac{1}{2\eta} \quad (3)$$

$$\omega = \frac{\mu^2}{2\eta} \quad (4)$$

The adsorption energy is calculated using eqn (5).

$$E_{ads} = E_{(molecule+Sb_3TMO_6)} - E_{molecule} - E_{Sb_3TMO_6} \quad (5)$$

$E_{(molecule+Sb_3TMO_6)}$ is the total energy of the cluster and adsorbed gas molecule structures and $E_{(molecule)}$ and $E_{Sb_3TMO_6}$ are the energies of the individual structures. The recovery time τ of a gas sensor is determined from the adsorption energy using eqn (6):

$$\tau = \nu^{-1} \exp\left(\frac{E_{ads}}{K_b T}\right) \quad (6)$$

where τ is the recovery time (s), *i.e.*, the time necessary for the gas molecule to desorb from the sensor surface, and ν is the typical vibration frequency of the adsorbed molecule on the surface.

Quantum topology of atoms in molecule (QTAIM) is used for the bonding analysis. Some main points were utilized in order to calculate the charge-transfer integral (CTI). The first step was to make fragments of the regions in which charge transfer was calculated, after which electronic coupling was computed for both the electrons and holes.

3. Results and discussions

The findings obtained after examining the structural, electronic and transport properties of $Sb_3(TM)O_6$ (where TM = Sc, Ti, V, Cr, Mn, Fe, Ni, and Co) as well as the adsorptions of the CO_2, SO_2, NH_3 and CH_4 molecules for gas sensing, are discussed. DFT calculations were carried out in order to investigate the $Sb_3(TM)O_6$ cage material for the potential gas-sensing application.

3.1. Suitable doping sites

Sb_4O_6 is an inorganic molecular cage structure existing as an isolated molecular cage rather than as conventional molecular clusters. Considering its unique 0D structure, the bonding and structure–property relationship is investigated in detail.[2] The results revealed that Sb_4O_6 completely satisfies its bonding requirements and does not require further bonding with any other atoms, due to which they are known as nearly inert cage materials. Sb_4O_6 consists of four atoms of antimony and six atoms of oxygen. Each Sb atom is surrounded by three atoms of oxygen.

For the application of such a cage material, each antimony atom was doped using a transition metal (TM) to yield eight new modified materials: Sb_3SCO_6, Sb_3TiO_6, Sb_3VO_6, Sb_3CrO_6, Sb_3MnO_6, Sb_3FeO_6, Sb_3CoO_6 and Sb_3NiO_6. To find the most stable doping site, each TM was placed in four distinct sites, A, B, C and D, and the doping site with minimum energy was identified. Sb(5) atom is named as site A, Sb(6) is named as B site, Sb(8) is marked as site C and Sb(10) is marked as site D, as shown in Fig. 1. Firstly, scandium (Sc) is placed in four available doping sites. The bonding energies for A, B, C and D are −2.721, −2.720, −2.719 and −2.716 eV, respectively. This revealed that for site A, Sb(6) has the minimum calculated energy. Similarly, the best doping sites for Ti, V, Cr, Mn, Fe, Ni and Co were determined to be B, D, B, A, B, A and C, respectively. The energy of each site is given in Table S1.

3.2. Structural properties

The optimized structure of Sb_3ScO_6 is represented in Fig. 2(a) which shows that the calculated Sb–O bond length is 1.99 Å, the O–Sc bond length is 1.90 Å and the Sc–O bond length is 1.91 Å. The dihedral bond angle of Sb–Sc–O is 123°, O–Sc–O is 104° and O–Sb–O is 96°. The calculated bonding energy is −74.42 eV. According to the Hirshfeld charge analysis, the total atomic charge on O is −2.627*e* and the charges on Sb and Sc are

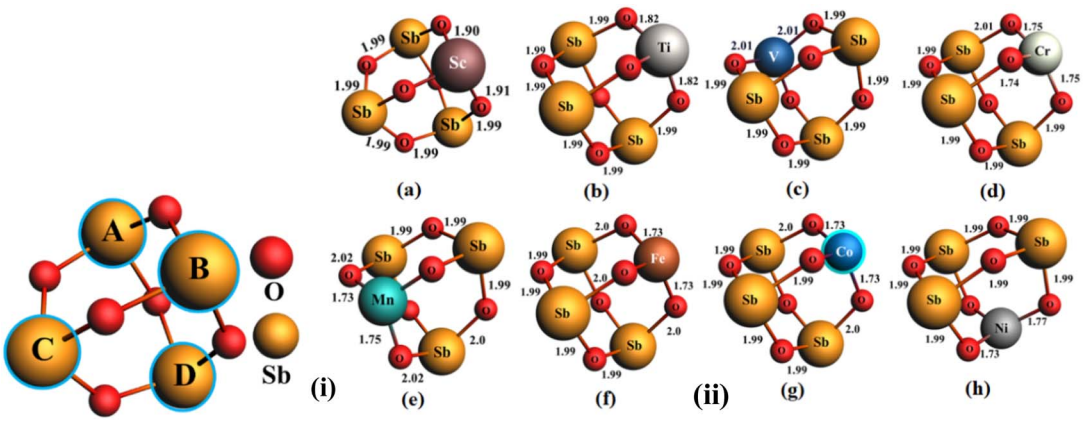

Fig. 1 Representation of the (i) doping sites and (ii) optimized structure of $Sb_3(TM)O_6$ (a), Sb_3ScO_6 (b), Sb_3TiO_6 (c), Sb_3VO_6 (d), Sb_3CrO_6 (e), Sb_3MnO_6 (f), Sb_3CoO_6 (g), Sb_3FeO_6 and (h) Sb_3NiO_6.

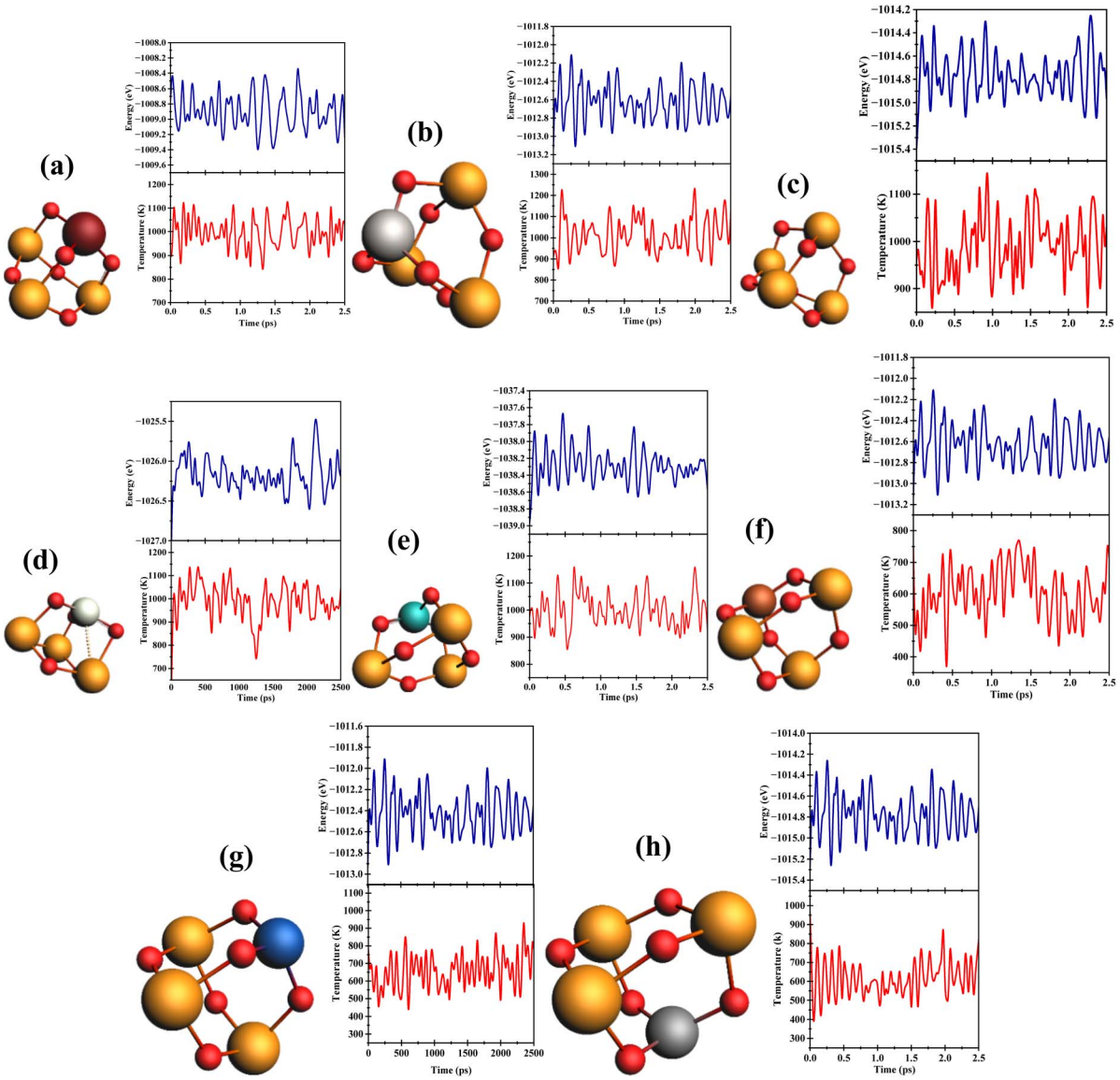

Fig. 2 Snapshots of $Sb_3(TM)O_6$ after AIMD simulation at 1000 K, along with graphs showing the change in energy and temperature over time for (a) Sb_3ScO_6, (b) Sb_3TiO_6, (c) Sb_3VO_6, (d) Sb_3CrO_6, (e) Sb_3MnO_6, (f) Sb_3FeO_6, (g) Sb_3NiO_6, and (h) Sb_3CoO_6.

−0.619*e* and 0.7695*e*, respectively. The computed values of the dipole moment in the *XYZ* plane are 2.70, 1.89 and 1.09 debye respectively. The calculated values of the quadrupole moment are −1.85 (quad-*xx*), 3.05 (quad-*xy*), 8.22 (quad-*xz*), −0.60 (quad-*yy*), 6.45 (quad-*yz*) and 2.45 (quad-*zz*), respectively. The optimized structure of Sb_3TiO_6 is represented in Fig. 2(b). The calculated bond length for O–Ti is 182 Å, O–Sb is 200 Å and Ti–O is 182 Å. The computed dihedral angle of O–Ti–O is 109°, O–Sb–O is 98° and Sb–O–Sb is 130°. The calculated bonding energy is −75.37 eV, and the net atomic charge on O is −2.45*e*, whereas the total charges on Sb and Ti are 1.95*e* and 0.50*e*, respectively. The calculated dipole moments in the *XYZ* plane are −1.08, −0.81 and −0.45 debye. On the other hand, the quadrupole moments are 1.09 (quad-*xx*), −052 (quad-*xy*), −2.96 (quad-*xz*), 0.26 (quad-*yy*), −2.44 (quad-*yz*) and −1.36 (quad-*zz*). The optimized structure of Sb_3VO_6 is illustrated in Fig. 2(c), which reveals that the bond length of O–V is 2.01 Å, V–O is 2.0 Å and Sb–O is 1.99 Å, while the bond angles of O–V–O is 113°, O–Sb–O is 97° and Sb–O–Sb is 130°, respectively. The net atomic charge on O is 01.95*e*, and the total charges on Sb and V are 1.97*e* and 0.38*e*, whereas the bonding energy is −76.80 eV. The calculated dipole moments in the *XYZ* plane are 1.21, −1.25 and 1.65 debye while the quadrupole moments are −4.72 (quad-*xx*), 4.06 (quad-*xy*), −3.87 (quad-*xz*), 0.81 (quad-*yy*), 0.10 (quad-*yz*) and 3.90 (quad-*zz*).

The optimized structure of Sb_3CrO_6 is shown in Fig. 2(d), which reveals that the bond length of O–Sb is 1.99 Å, O–Cr is 1.75 Å and Cr–O is 1.75 Å, while the bond angle of O–Sb–O is 96°, O–Cr–O is 113° and Sb–O–Sb is 130°. The net atomic charge on O is 1.60*e*, while the total charges on Sb and Cr are 1.97*e* and 0.38*e*, respectively. The calculated bonding energy is −76.80 eV while the dipole moments in the *XYZ* plane are 1.21, −1.25, and

1.65 debye. The quadrupole moments are −4.72 (quad-*xx*), 4.06 (quad-*xy*), −3.87 (quad-*xz*), 0.81 (quad-*yy*), 0.10 (quad-*yz*) and 3.90 (quad-*zz*), respectively. The optimized structure of Sb_3MnO_6 is represented in Fig. 2(e). The results reveal that the bond length of O–Sb is 2.02 Å, Mn–O is 1.75 Å and Sb–O is 2 Å, while the bond angle of O–Mn–O is 110°, O–Sb–O is 96°, and Sb–O–Sb is 130°. The net atomic charge on O is −2.26*e*, while the total charges on Sb and Mn are 1.95*e* and 0.31*e*, respectively, whereas the bonding energy is −76.10 eV. The calculated dipole moments in the *XYZ* plane are 1.33, 0.95, and 1.73 debye, while the calculated quadrupole moments are −0.30 (quad-*xx*), −3.74 (quad-*xy*), 1.20 (quad-*xz*), 5.95 (quad-*yy*), 4.73 (quad-*yz*), and −5.64 (quad-*zz*). The optimized structure of Sb_3FeO_6 is represented in Fig. 2(f). The calculated bond length of O–Sb is 1.99 Å, Sb–O is 2 Å and Fe–O is 1.73 Å, while the dihedral angle of O–Sb–O is 97, Sb–O–Sb is 130 and O–Fe–O is 114. The net atomic charge on O is −2.25*e*, while the total charges on Sb and Fe are 1.93*e* and 0.31*e*, respectively. The calculated bonding energy is −74.93 eV, while the dipole moments in the *XYZ* plane are −1.26, −1.08 and −0.68 debye. The quadrupole moments are 1.10 (quad-*xx*), −0.84 (quad-*xy*), −3.50 (quad-*xz*), 0.75 (quad-*yy*), −3.21 (quad-*yz*) and −1.85 (quad-*zz*).

The optimized structure of Sb_3CoO_6 is shown in Fig. 2(g). The results reveal that the bond length of O–Sb is 199 Å, Ni–O is 1.77 Å, and Sb–O is 1.99 Å, while the bond angle of O–Co–O is 111°, O–Sb–O is 96° and Sb–O–Sb is 129°, respectively. The net atomic charge on O is −2.25*e*, while the total charges on Sb and Fe are 1.93*e* and 0.31*e*, respectively. The bonding energy is −74.65 eV. The net atomic charge on O is −2.86*e*, while the total charges on Sb and Co are 1.73*e* and 0.38*e*, respectively. The calculated dipole moments in the *XYZ* plane are 1.12, −0.83 and −0.44 debye while the calculated quadrupole moments are 0.87 (quad-*xx*), −0.91 (quad-*xy*), −3.30 (quad-*xz*), 0.25 (quad-*yy*), 2.66 (quad-*yz*) and −1.12 (quad-*zz*). The optimized structure of Sb_3NiO_6 is illustrated in Fig. 2(h), which reveals that the bond length of O–Ni is 1.77 Å, Ni–O is 1.73 Å and Sb–O is 1.99 Å, while the bond angle of O–Ni–O is 108°, O–Sb–O is 97° and Sb–O–Sb is 130°, respectively. The net atomic charge on O is −2.38*e*, while the total charges on Sb and Ni are 1.90*e* and 0.49*e*, respectively. The results reveal that the bonding energy is −68.63 eV. The calculated dipole moments in the *XYZ* plane are −0.65, 1.82 and 0.77 debye, whereas the quadrupole moments are 2.69 (quad-*xx*), 0.06 (quad-*xy*), −2.04 (quad-*xz*), −6.50 (quad-*yy*), 0.16 (quad-*yz*) and 3.81 (quad-*zz*). The detailed structural properties of all modified clusters are mentioned in Table S2 of the SI file.

3.3. Stability of the doped Sb_3 (TM)O_6 material through AIMD simulation

The Sb_3TMO_6 cluster configurations are evaluated for stability. The adsorption energy is taken as the energy difference between a system of an atom or molecule deposited on a structure and the overall energy of the adsorbent and the adsorbate. *Ab initio* molecular dynamics (AIMD) simulations were carried out at a high temperature of 1000 K for 25 ps, with the plots of temperature and energy against time illustrated in Fig. 2.

The AIMD simulation of Sb_3ScO_6 was performed using a cell containing 3 antimony (Sb), 1 scandium (Sc) and 6 oxygen (O) atoms, while the Sb_3TiO_6 cell contained 3 antimony (Sb), 1 titanium (Ti) and 6 oxygen (O) atoms and the structure after the simulation is shown in Fig. 2(a) and (b). Similarly, the Sb_3VO_6, Sb_3CrO_6, Sb_3MnO_6, Sb_3FeO_6, Sb_3NiO_6 and Sb_3CoO_6 structures after simulation are represented in Fig. 2(c), (d), (e), (f), (g) and (h), respectively. The energy of all the systems remained rather constant throughout the simulations, and structural analysis showed that there is no bond breakage which indicates the stability of the materials.

3.4. Electronic properties

The frontier molecular orbitals (FMOs) of the molecule consist of the highest occupied molecular orbital (HOMO) and the lowest unoccupied molecular orbital (LUMO). FMOs are crucial for determining the interactions that occur between the molecules *via* the analysis of the relevant electronic spectra.[53] A molecule's chemical reactivity, kinetic stability and chemical hardness/softness are determined by the energy gap between its HOMO and LUMO. Another effective gauge for chemical stability is chemical hardness. Large-energy-gap molecules are typically referred to as hard molecules, while those with insignificant energy gaps are referred to as soft molecules. Because they require lower energy for excitation than hard molecules, soft molecules are more polarizable than hard ones.[54] The calculated HOMO and LUMO energies for Sb_3ScO_6 are −7.17 and −4.9 eV, respectively, as shown in Fig. 3(a). The orbital contributions to the HOMO from Sb, Sc, and O are 35.56, 51.56, and 15.94%. LUMO contains 50.96% contribution from Sc, 19.61% from Sb and 6.34% from oxygen. The computed chemical hardness (η), chemical softness (S), chemical potential (μ), conductivity (ΔE) and electrophilicity (ω) of Sb_3ScO_6 are 2.47 eV, 0.40 eV^{-1}, −4.69 eV, 4.95 eV, and 4.45 eV respectively. The hardness value is greater than 2 eV, which concludes that Sb_3ScO_6 is a hard material class. In the case of partial contribution of s, p and d orbitals of each constituent atom, the p orbital has the highest DOS contribution near the Fermi level and is responsible for the chemical properties. For Sb_3TiO_6, the computed HOMO and LUMO energies are −7.79 and −3.44 eV, respectively, as shown in Fig. 3(b). The contributions of Sb, Ti, and O to the HOMO are 46.22%, 1.30%, and 47.05% respectively. The composition of the LUMO is 21.39% Ti, 72.37% Sb and 7.24% O. The p orbital contributes the highest to the DOS in the case of Sb and O, and for O, the d orbital does not exist, but in the case of Ti, the d orbital contributes significantly to the DOS because of its electronic presence and reasonable energy values. The calculated values for the Sb_3TiO_6 are 2.17 eV, 0.46 eV^{-1}, −5.61 eV, 4.35 eV and 7.25 eV for η, S, μ, conductivity (ΔE) and ω, respectively. Since the hardness value is larger than 2 eV, Sb_3TiO_6 has been identified as a hard material. The calculated HOMO and LUMO energies for Sb_3VO_6 are −4.52 and −2.01 eV, respectively, as shown in Fig. 3(c). The HOMO contributions from V, Sb and O are 35.56%, 89.98% and 4.89%, respectively. The LUMO contains 48.28% contribution from V, 41.58% from Sb and 3.96% from oxygen. Sb_3VO_6 exhibited η, S, μ, ΔE and ω

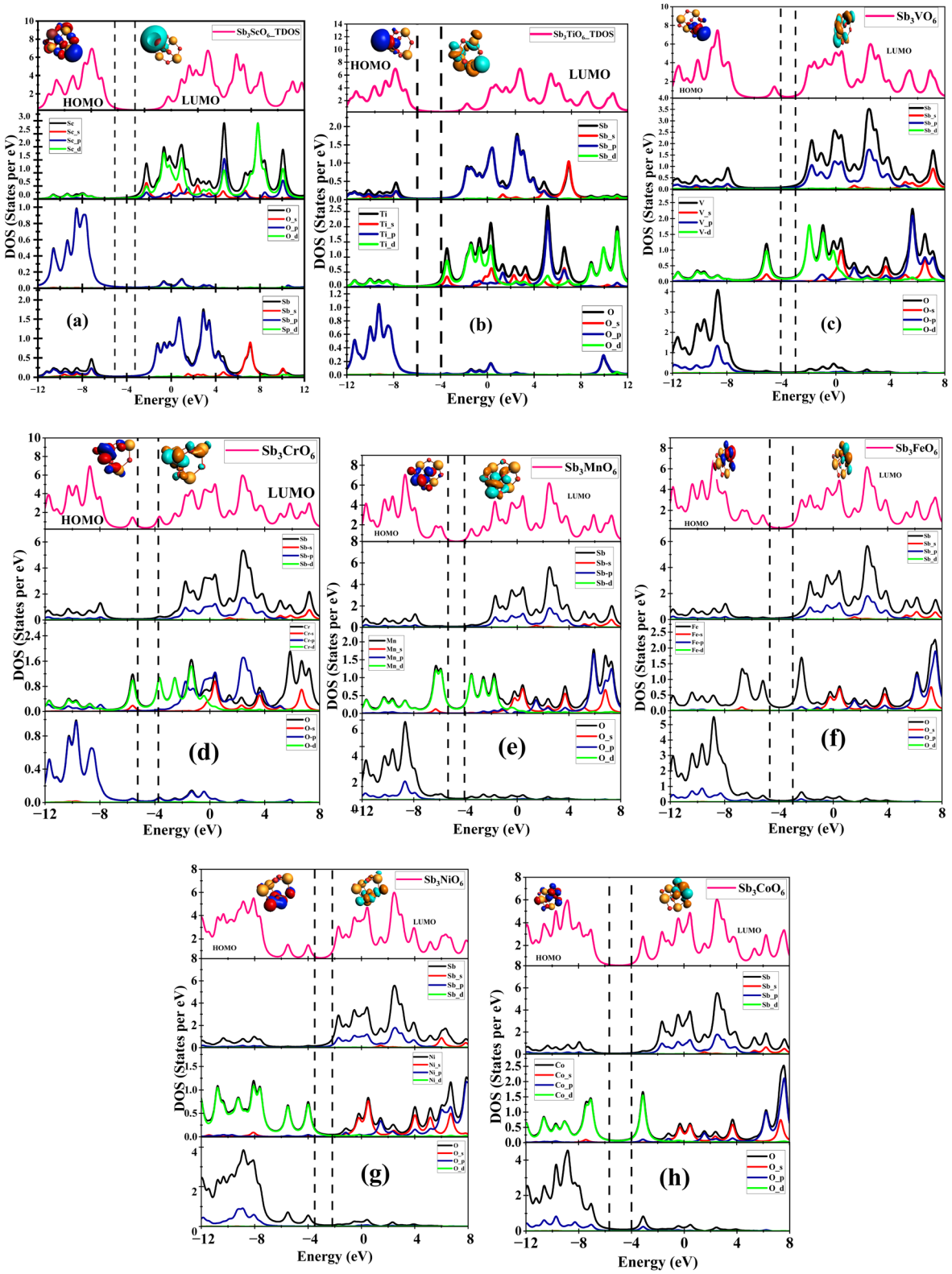

Fig. 3 Calculated electronic properties of (a) Sb_3ScO_6, (b) Sb_3TiO_6, (c) Sb_3VO_6, (d) Sb_3CrO_6, (e) Sb_3MnO_6, (f) Sb_3FeO_6, (g) Sb_3NiO_6, and (h) Sb_3CoO_6.

values of 1.25 eV, 0.79 eV^{-1}, −3.26 eV, 2.51 eV, and 4.25 eV, respectively. The hardness value is less than 2 eV, which indicates that Sb_3VO_6 is a soft material. For Sb_3CrO_6, the computed HOMO and LUMO energies are −5.62 and −3.67 eV, respectively, as shown in Fig. 3(d). The calculated HOMO–LUMO gap is 1.94 eV. The contributions of Cr and O to the HOMO are

87.76% and 5.17%, respectively. The LUMO is composed of 76.6% Cr, 9.4% Sb and 8.68% O. The calculated η, S, μ, ΔE and ω values for Sb_3TiO_6 are 0.47 eV, 2.10 eV^{-1}, −4.14 eV, 0.95 eV and 18.08 eV, respectively. Since the hardness value is less than 2 eV, Sb_3CrO_6 has been identified as a soft material.

The calculated HOMO and LUMO energy levels for Sb_3MnO_6 are −5.88 and −3.54 eV, respectively as shown in Fig. 3(e). The contributions to the HOMO from Mn, Sb and O are 71.58%, 2.28% and 18.27% respectively. The LUMO contains 80.02% contribution from Mn, 7.24% from Sb and 7.36% from oxygen. The computed η, S, μ, ΔE and ω values for Sb_3MnO_6 are1.17 eV, 0.85 eV^{-1}, −4.71 eV, 2.34 eV and 9.48 eV respectively. The hardness value is less than 2 eV, which indicates that Sb_3VO_6 is a soft material.

For Sb_3FeO_6, the computed HOMO and LUMO energies are −6.33 and −5.17 eV, respectively as shown in Fig. 3(f). The contributions of Sb, Fe and O to the HOMO are 3.65%, 61.30% and 23.83%, respectively. The LUMO is composed of 21.39% Ti, 72.37% Sb and 7.82% O. The calculated η, S, μ, ΔE and ω values for the Sb_3FeO_6 are 0.58 eV, 1.72 eV^{-1}, −5.75 eV, 1.16 eV and 28.53 eV respectively. Since the hardness value is less than 2 eV Sb_3FeO_6 has been identified as a soft material.

The calculated HOMO and LUMO energy levels for Sb_3NiO_6 are −7.57 and −5.51 eV, respectively, as shown in Fig. 3(g). The HOMO contributions from Ni, Sb, and O are 29.11%, 16.76% and 47.65%, respectively. The LUMO contains 52.82% contribution from Ni, 2.17% from Sb, and 36.39% from oxygen. The computed η, S, μ, ΔE and ω values for Sb_3NiO_6 are 1.03 eV, 0.97 eV^{-1}, −6.54 eV, 2.06 eV, and 20.76 eV, respectively. The hardness value is less than 2 eV, which indicates that Sb_3VO_6 is a soft material. For Sb_3CoO_6, the computed HOMO and LUMO energies are −7.04 and −3.11 eV, respectively, as shown in Fig. 3(h). The contributions of Sb, Co and O to the HOMO are 1.29%, 62.59% and 43.6%, respectively. The LUMO is composed of 59.46% Co, 1.26% Sb and 28% O. The calculated η, S, μ, ΔE and ω values for the Sb_3CoO_6 are 1.96 eV, 0.50 eV^{-1}, −5.07 eV, 3.93 eV and 6.55 eV, respectively. Since the hardness value is less than 2 eV, Sb_3CoO_6 has been identified as a soft material. By analysing the partial density of states PDOS, it is revealed that the p orbital of antimony Sb, the p orbital of oxygen O, have major contributions while the p orbital of TM contributes mainly. For all the $Sb_3(TM)O_6$ cages, the contributions of Sb and O remain the same, and partial DOS analysis reveals that the p orbitals of both Sb and O show the highest-intensity peaks, indicating that they are the valence orbitals contributing to bonding. In the cases of Sb and O, the 5p and 2p orbitals, respectively, have the energy closest to the Fermi level; thus, they have the highest tendency to contribute to the bonding. The replacement of different TM atoms leads to the partial contribution of d-orbital is noted to be the highest in case of V, Cr, Mn, Fe, Ni, and Co as electrons reside in d-orbitals of all these atoms, and the 3d-orbital is much narrower than s and p ones, which confines high density of states (DOS) and sharp energy range of all these atoms.

The total and partial DOSs of the CO_2-adsorbed Sb_2O_3 monolayers calculated using different dopants in order to better comprehend the electronic component are shown in Fig. 3(a)–(e). The DOS curves reveal that with CO_2 adsorption, transition-metal dopants with partially filled d-orbitals (V, Cr, and Mn) cause significant changes close to the Fermi level, which are evidenced by the noticeable hybridization peaks in both the HOMO and LUMO regions. These characteristics indicate a stronger electronic interaction between the dopant-centered states and the CO_2 molecule orbitals, leading to improved charge transfer and more stable adsorption. Sc- and Ti-doped systems, on the other hand, show relatively slight DOS variations with minimal orbital overlap and minimal modification around the Fermi level, indicating weaker physisorption interactions. The stronger chemisorption is further demonstrated by the observed shifts of the HOMO towards the Fermi level and the increasing size of the LUMO region in the Cr- and Mn-doped systems. Overall, the DOS analysis verifies that the degree of orbital hybridization and the degree of electronic interaction between CO_2 and the dopant-modified Sb_2O_3 monolayers are responsible for the selective sensing capabilities. TM-modified DOS hybridization improves CO_2 adsorption by improving charge transfer and electronic coupling, according to research findings on doped graphene, MgO, WS_2, and metal oxides. These findings are supported by similar observations on CeO_2 and $SrTiO_3$, which demonstrate that such electronic disturbances are strong indications of chemisorption.[55–59] The calculated HOMO, LUMO and HOMO–LUMO gap for the clusters are given in Fig. S1.

3.5. Structural properties of gas molecules

The CO_2, SO_2, NH_3 and CH_4 molecules are optimized with the same parameters as those for the pure structure given in Fig. 4. The CO_2 molecule consists of two atoms of oxygen and one atom of carbon (C), which is named as carbon dioxide (CO_2). The bond length (C–O) of the CO_2 molecule is 1.16 Å, which agrees with reported results;[60] it has a linear geometry with a bond angle of 180°. The bond lengths of SO_2 are 1.44 Å and 1.70 Å, and it exhibits a linear geometry.[61]

In the case of the NH_3 molecule, the bond length is 1.02 Å, and the respective bond angle is 106°. In the case of CH_4, the length of each C–H bond is 1.08 Å, and the bond angle is 109°, as shown in Fig. 4.[62,63]

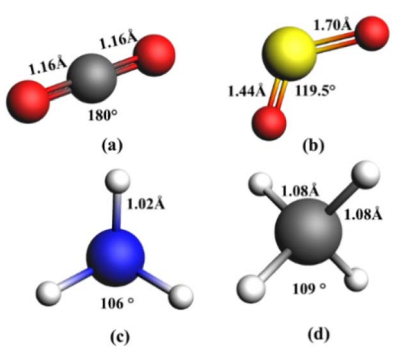

Fig. 4 Optimized structures showing the bond lengths and bond angles of (a) CO_2, (b) SO_2, (c) NH_3 and (d) CH_4.

3.6. CO_2 gas adsorption on $Sb_3(TM)O_6$

In order to describe the gas-sensing behavior of $Sb_3(TM)O_6$, the adsorption behavior of individual structures of the clusters needs to be analyzed. To adsorb gas molecules on $Sb_3(TM)O_6$, finding the most stable adsorption site is important. Considering the nearly inert nature of Sb_3O_6, the bonding sites of antimony and oxygen do not allow any molecule to interact with them.[64] However, the TM site allows interactions with the gas molecules. On the other hand, the most favorable adsorption sites are found by performing different single-point calculations for different configurations of molecules, and the most favorable will be the one with the least energy of bonding. The molecules for which the adsorption energy is less than <-0.5 eV are regarded to have a weak interaction, whereas those with an adsorption energy >-0.5 eV have a strong interaction.

The optimized structures of Sb_3ScO_6 with CO_2 gas molecule adsorption on the structure are shown in Fig. 5(a). CO_2 is a triatomic molecule comprising one carbon and two oxygen atoms, where each of the oxygen atoms is covalently double-bonded with two valence electrons of the oxygen atom. The CO_2 molecule has a linear geometry, and the bonding angle between the oxygen atom from the CO_2 molecule and the C atom in the Sb_3ScO_6 structure is 180°, as shown in Fig. 5(a). The adsorption energy is −0.81 eV, which shows the good interaction of the host with the guest molecule. The optimized distance between Sc and the O atom is 2.39 Å. The structure of the gas molecule after adsorption shows an increase in its bond length, and the bond length after elongation is 1.17 Å. The optimized structures of Sb_3TiO_6 with a CO_2 gas molecule adsorbed on the structure are shown in Fig. 5(b). The adsorption energy is calculated using eqn (6). The adsorbed energy has a low value in this case, which is −0.06 eV, whereas the vertical distance is 4.13 Å. The findings exhibit a weak interaction between the host and CO molecule, which points to physisorption and, hence, the absence of any change in the structure of the host. The vanadium atom forms a bond with carbon, and the distance between them is 1.81 Å. The optimized structures of Sb_3VO_6 with a CO_2 gas molecule adsorbed on the structure are shown in Fig. 5(c). The adsorption energy is −0.19 eV, which shows the good interaction of the host with the guest molecule. The optimized distance between the V and O atoms is 2.0 Å. The structure of the gas molecule after adsorption shows the increase in its bond length, and the bond length after elongation is 1.17 Å, whereas the calculated bond angle after adsorption is 142°. The sum of the radii of connected atoms is less than their bonding distance, which points to a weak type of interaction, such as physisorption.

The optimized structures of Sb_3CrO_6 with a CO_2 gas molecule adsorbed on the structure are shown in Fig. 5(d). The adsorption energy is calculated as −0.09 eV, whereas the vertical distance is 4.03 Å. The findings indicate a very weak type of interaction, *i.e.*, physisorption, due to which no change in the structure of the host takes place.

The optimized structures of Sb_3MnO_6 with a CO_2 gas molecule adsorbed on the structure are shown in Fig. 5(e). The adsorption energy is −0.40 eV, which shows the good interaction of the host with the guest molecule. The optimized distance between Mn and the O atom is 2 Å. The structure of the gas molecule after adsorption shows an increase in its bond length, and the bond length after elongation is 1.17 Å. The sum of the radii of connected atoms is less than their bonding distance; thus, a weak type of interaction in the form of physisorption takes place. The optimized structures of Sb_3FeO_6, Sb_3NiO_6 and Sb_3CoO_6 with CO_2 gas molecule adsorbed on the structure are shown in Fig. 5(e)–(g). The adsorption energy appears low with values of −0.06, −0.40 and 0.06 eV, and the vertical distances are large, 3.85, 4.03 and 4.52 Å. These findings show a very weak interaction between the host and guest molecule in the form of physisorption, and hence, no change in the structure of the host takes place. The summarized results of the CO_2 gas adsorption are mentioned in Table S3.

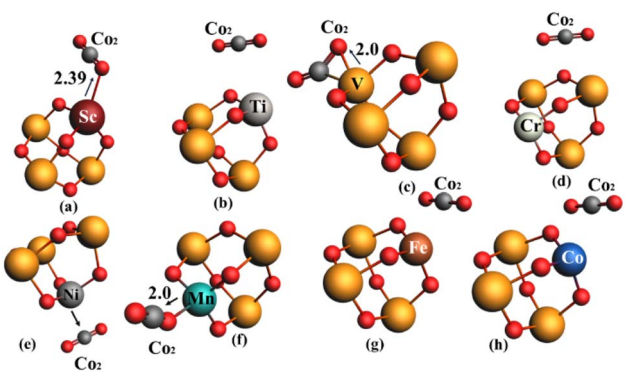

Fig. 5 CO_2 gas adsorption on the cage molecular material: (a) Sb_3ScO_6, (b) Sb_3TiO_6, (c) Sb_3VO_6, (d) Sb_3CrO_6, (e) Sb_3MnO_6, (f) Sb_3FeO_6, (g) Sb_3NiO_6, and (h) Sb_3CoO_6.

3.7. Electronic properties after the adsorption of CO_2

The calculated HOMO and LUMO energies for the CO_2-adsorbed Sb_3ScO_6 cluster are −7.11 and −1.44 eV, respectively, as shown in Fig. 6(a). The contributions to the HOMO from Sb, Sc and O are 47.81%, 1.31% and 45.48%. The LUMO contains 84.10% contribution from Sc, 4.74% from Sb, 0.56 from C and 1.22% from O. The Sb_3ScO_6 cluster exhibited ω values of 2.83 eV, 0.35 eV, 0.35 eV, −4.27 eV, and 3.22 eV, respectively. The hardness value is greater than 2 eV, indicating that the CO_2-adsorbed Sb_3ScO_6 is a hard material. For Sb_3TiO_6–CO_2, the computed HOMO and LUMO energies are −7.82 and −3.46 eV, respectively, as shown in Fig. 6(b). The contributions of Sb, Ti, and O to the HOMO are 49.32%, 0.22%, and 47.81%, respectively. The LUMO is composed of 95.28% Ti. The calculated η, S, μ, ΔE, and ω values for the Sb_3TiO_6 are 2.18 eV, 0.45 eV^{-1}, −5.64 eV, 0.45 eV and 7.30 eV, respectively. Since the hardness value is larger than 2 eV, Sb_3TiO_6 has been identified as a hard material. The calculated HOMO and LUMO energies for Sb_3VO_6–CO_2 are −5.15 and −2.10 eV, respectively, as shown in Fig. 6(c). The HOMO has 66.07% and 24.04% contributions from V and Sb, respectively. The LUMO has 68.07% contribution from V and 24.04% from Sb. The values of η, S, μ, ΔE, and ω for Sb_3ScO_6 are 1.52 eV, 0.65 eV^{-1}, −3.62 eV, 0.65 eV, and 4.31 eV, respectively. The hardness value is less than 2 eV, which

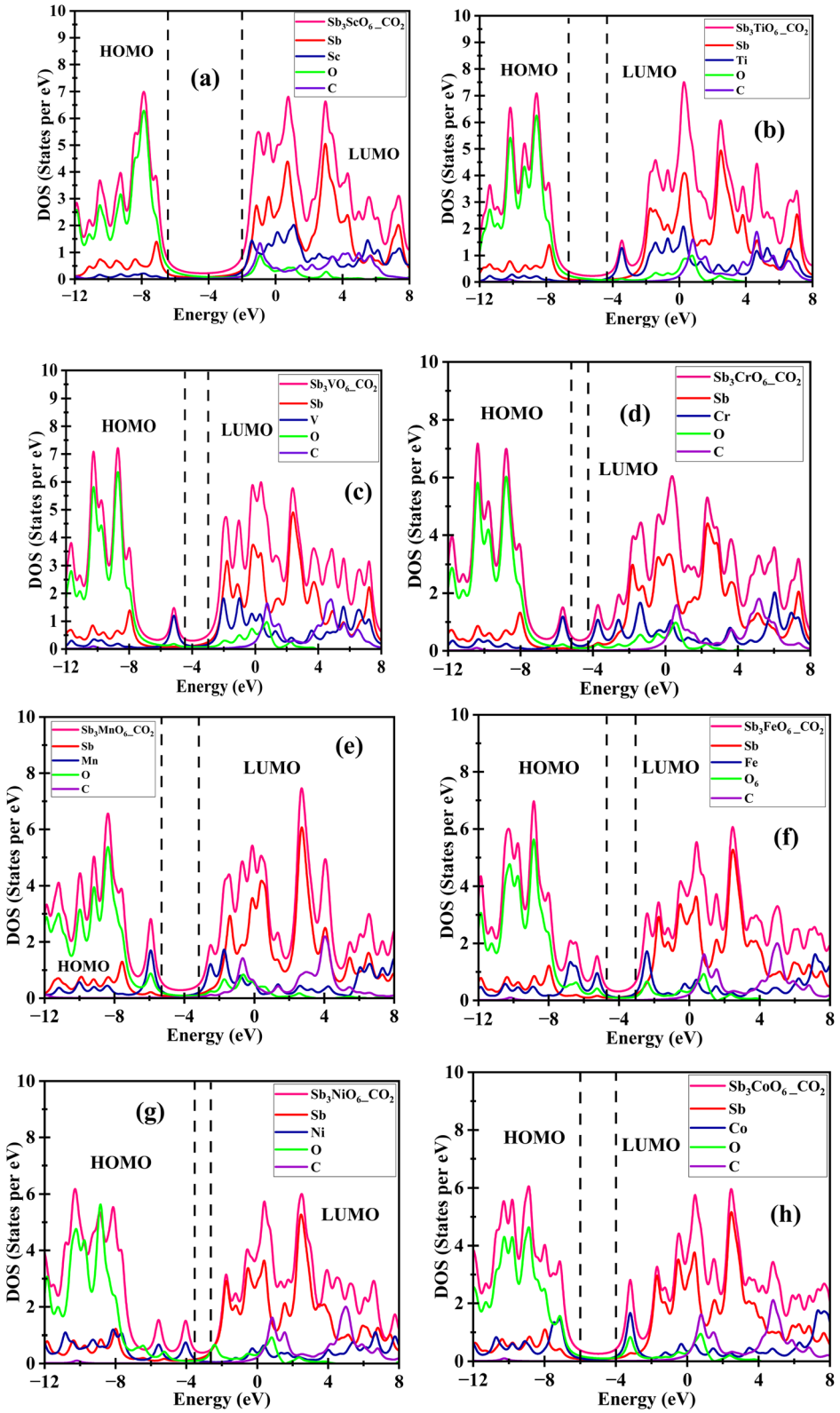

Fig. 6 Calculated electronic properties for the CO_2-adsorbed $Sb_3(TM)O_6$ (where TM is Sc, Ti, V, Cr, Mn, Fe, Ni, and Co): (a) Sb_3ScO_6, (b) Sb_3TiO_6, (c) Sb_3VO_6, (d) Sb_3CrO_6, (e) Sb_3MnO_6, (f) Sb_3FeO_6, (g) Sb_3NiO_6, and (h) Sb_3CoO_6.

indicates that the CO_2-adsorbed Sb_3VO_6 is a soft material. For Sb_3CrO_6–CO_2, the computed HOMO and LUMO energies are −5.67 and −3.72 eV, respectively, as shown in Fig. 6(d). The contributions of Ti and O to HOMO are 87.75% and 5.22%, respectively. The LUMO is composed of 9.24% antimony, 77.05% chromium and oxygen 9.72%. The calculated values of η, S, μ, ΔE,

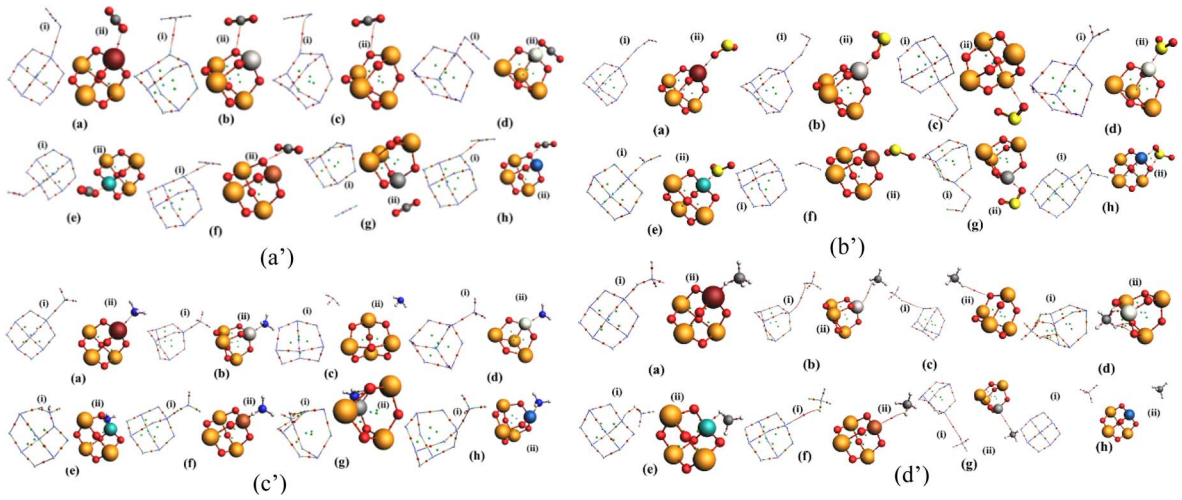

Fig. 7 QTAIM analysis of the $Sb_3(TM)O_6$ cages with (a′) CO_2, (b′) SO_2 (c′) NH_3 and (d′) CH_4 bonded. (i) Topology and (ii) ball and stick model.

and ω for the Sb_3CrO_6 are 0.97 eV, 1.02 eV^{-1}, −4.69 eV, 1.02 eV and 11.30 eV, respectively. Since the hardness value is less than 2 eV, Sb_3CrO_6 has been identified as a soft material.

The calculated HOMO and LUMO energies for Sb_3MnO_6–CO_2 are −5.90 and −2.51 eV, respectively, as shown in Fig. 6(e). The HOMO contributions from Sb, Mn and O are 2.49%, 64.01% and 23.05%, respectively. LUMO contains 83.92% contribution of Mn, 81.56% contribution from the antimony Sb, carbon C has 4.43 and oxygen has 5.42%.

The Sb_3ScO_6 cluster exhibited η, S, μ, ΔE and ω values of 1.63 eV, 0.59 eV^{-1}, 4.20 eV, 0.59 eV, and −5.22 eV, respectively. The hardness value is less than 2 eV, which indicates that the CO_2-adsorbed Sb_3MnO_6 is a soft material. For the CO_2-adsorbed Sb_3FeO_6 system, the computed HOMO and LUMO energies are −6.42 and −5.24 eV, respectively, as shown in Fig. 6(f). The contributions of Sb, Fe, and O to the HOMO are 3.65%, 61.2% and 4.36%, respectively. The LUMO is composed of 66.14% Fe, 4.35% Sb and 21.47% oxygen. The calculated η, S, μ, ΔE and ω values for the Sb_3FeO_6 are 0.59 eV, 1.69 eV^{-1}, −5.83 eV, 1.69 eV and 28.81 eV, respectively. The large value of hardness in the case of Sb_3TiO_6 indicates that it is a hard material.

The calculated HOMO and LUMO energies for the CO_2-adsorbed Sb_3NiO_6 are −7.63 and −5.56 eV, respectively, as shown in Fig. 6(g). The HOMO contributions from Ni, Sb and O are 29.63%, 11.71% and 48.36%, respectively. The LUMO contains 52.82% contribution from Ni, 2.16% from Sb, and 36.47% from O. The Sb_3NiO_6 cluster exhibited η, S, μ, ΔE and ω values of 1.03 eV, 0.96 eV^{-1}, −6.54 eV, 0.96 eV, and 21 eV, respectively. The hardness value is less than 2 eV, which indicates that the CO_2-adsorbed Sb_3VO_6 is a soft material. For Sb_3CoO_6, the computed HOMO and LUMO energies are −7.11 and −3.19 eV, respectively, as shown in Fig. 6(h). The contributions of Sb, Co and O to the HOMO are 7.7%, 43.3% and 47.98%, respectively. The LUMO is composed of 63.84% Co, 1.18% Sb and 29.7% O. The calculated η, S, μ, ΔE and ω values for Sb_3CoO_6 are 1.96 eV, 0.51 eV^{-1}, −5.15 eV, 3.91 eV and 6.77 eV, respectively. Since the hardness value is less than 2 eV, Sb_3CoO_6 has been identified as a soft material.

3.8. Quantum topology of atoms in molecule (QTAIM)

The QTAIM calculation points to the splitting of the molecule density in line with Bader theory-based zero-flux surfaces. It sheds light on the binding path and topology of the entire system rather than a simple bond path. Fig. 7(a′) provides the topology of the entire system composed of CO_2 gas molecules absorbed on the Sb_3TMO_6 cages based on the QTAIM analysis. In the present illustration, the ring critical point and cage critical point are represented by green and light blue colors, while the bond critical point (BCP) and atom critical point (ACP) are represented by red and white colors, respectively. The QTAIM diagram with its specific structure is displayed in Fig. 7(b′), which provides the topology of the entire system composed of SO_2 gas molecules absorbed on the Sb_3TMO_6 cages, where (i) shows the topology and (ii) shows the ball and stick model in each case. In the same way, Fig. 7(c′) and (d′) represent the QTAIM analysis of NH_3 and CH_4 absorbed on all eight cages of Sb_3TMO_6, respectively.

The bonding inside the cage points to a strong interaction on the basis of the small distance between the atom critical points. Conversely, the bonding between the CO_2 molecule and the host material has a large distance, which points to a weak interaction.

3.9. Stability of the fully loaded structure of the CO_2-adsorbed host through AIMD simulations

The stability levels of the CO_2-absorbed Sb_3ScO_6, Sb_3VO_6, and Sb_3MnO_6 are demonstrated in Fig. 8(a)–(c), which shows a snapshot after absorption and the change in energy and temperature over the time interval. The AIMD simulations were performed for 25 ps to know the stability of the CO_2-adsorbed Sb_3TMO_6 structure, with temperature and energy plotted against time, as illustrated in Fig. 8. The energy of all systems remained unchanged with very low fluctuations over the simulations, as shown in Fig. 8(a) and (b); in some cases, it reduces to relax the structure after the absorption of CO_2, as shown in Fig. 8(c). The energy does not show a typical constant

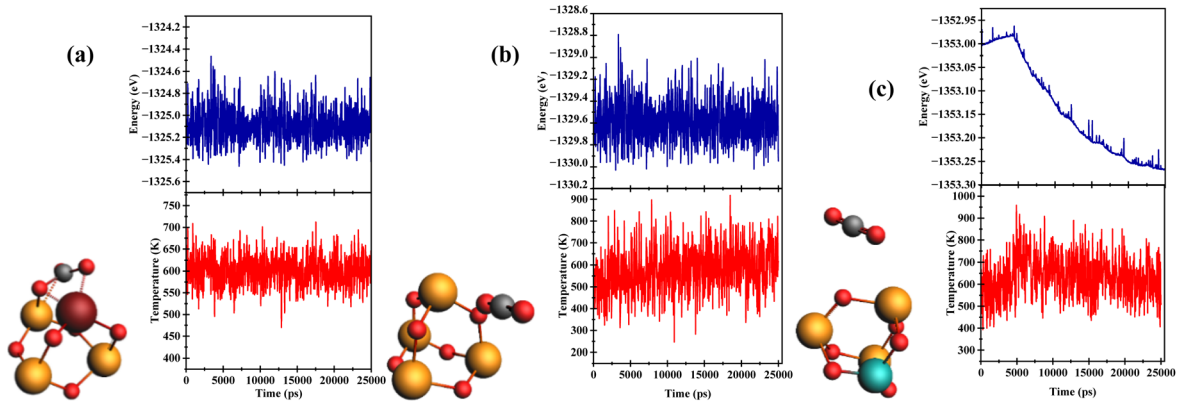

Fig. 8 AIMD Simulation of the fully loaded CO_2-absorbed (a) Sb_3ScO_6, (b) Sb_3VO_6, and (c) Sb_3MnO_6.

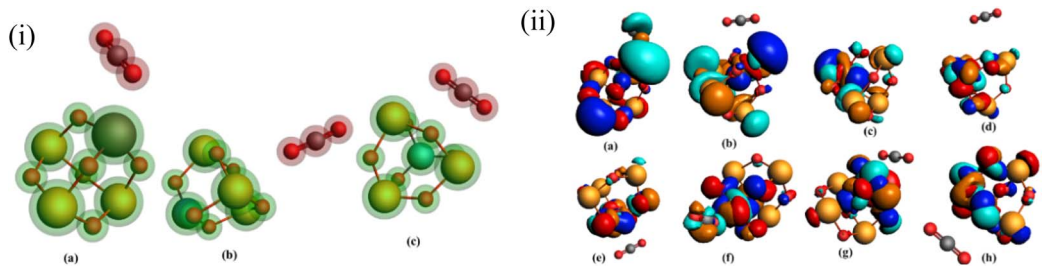

Fig. 9 Visual representation of charge transfer of Sb_3TMO_6 (i) fragments (ii) HOMO–LUMO.

trend because, unlike the other two cases, here, CO_2 has not formed a bond with Sb_3MnO_6 at the equilibrium position. The snapshots of the structures are displayed in Fig. 8, which indicates the stability of the materials on the basis of the absence of any bond breakage.

3.10. Charge transfer integral

In order to perform charge-transfer integral (CTI) calculations, two fragments were considered, as shown in Fig. 9. The CO_2 molecule is taken as region 1, while the Sb_3TMO_6 cage material is taken as region 2.

The calculations indicated that Sb_3ScO_6 exhibits electron- and hole-transfer energies of 0.22 eV and 0.05 eV, respectively, and the recombination energy from fragment 1 to fragment 2 was 0.45 eV, while the recombination energy from fragment 2 to 1 was 0.42 eV. In the case of Sb_3VO_6, the electron- and hole-transfer energies are 0.21 eV and 0.01 eV, respectively, and the recombination energy from fragment 1 to fragment 2 is 0.009 eV, while the recombination energy from fragment 2 to 1 is 0.04 eV. For Sb_3MnO_6, the calculated electron- and hole-transfer energies are 0.04 eV and 0.1 eV, respectively, and the recombination energy from fragment 1 to fragment 2 is 0.04 eV, while the recombination energy from fragment 2 to 1 is 0.01 eV.

3.11. Adsorption of SO_2

The optimized structures of Sb_3ScO_6 with the SO_2 gas molecule adsorbed on the structure are shown in Fig. 10(a). The adsorption energy is −5.49 eV, which shows the good interaction of the host with the guest molecule. The optimized distance between Sc and the O atom is 2.33 Å. The structure of the gas molecule after adsorption shows an increase in its bond length, and the bond length after elongation is 1.46 Å. The sum of the radii of connected atoms is less than their bonding distance; thus, a weak type of interaction, *i.e.*, physisorption, takes place. The optimized structures of Sb_3TiO_6 with the SO_2 gas molecule adsorbed on the structure are shown in Fig. 10(b). The adsorption energy is −6.32 eV, which shows the good interaction of the host with the guest molecule. The optimized distance between Ti and the O atom is 1.89 Å. The structure of the gas molecule after adsorption shows an increase in its bond length, and the value of the bond length after elongation is 1.59

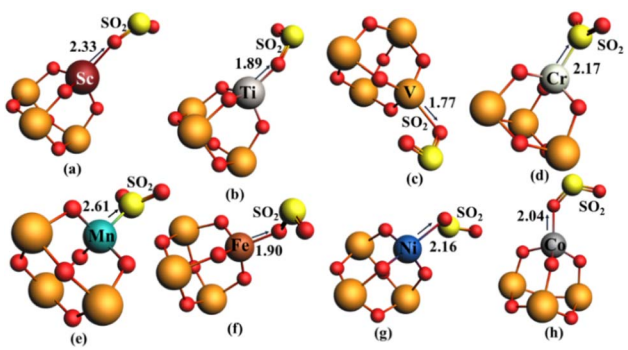

Fig. 10 Optimized structures of SO_2 gas-adsorbed (a) Sb_3ScO_6, (b) Sb_3TiO_6, (c) Sb_3VO_6, (d) Sb_3CrO_6, (e) Sb_3MnO_6, (f) Sb_3FeO_6, (g) Sb_3NiO_6 and (h) Sb_3CoO_6.

Å. The sum of the radii of connected atoms is less than their bonding distance; thus, a weak type of interaction, *i.e.*, physisorption, takes place. The optimized structures of Sb_3VO_6 with the SO_2 gas molecule adsorbed on the structure are shown in Fig. 10(c). The adsorption energy is −2.92 eV, which shows the good interaction of the host with the guest molecule. The optimized distance between the V and O atoms is 1.77 Å. The structure of the gas molecule after adsorption shows an increase in its bond length, and the bond length after elongation is 1.56 Å. The sum of the radii of connected atoms is greater than their bonding distance; thus, a strong type of interaction, *i.e.*, chemisorption, takes place. The optimized structures of Sb_3CrO_6 with the SO_2 gas molecule adsorbed on the structure are shown in Fig. 10(d). The adsorption energy is −5.03 eV, which shows the good interaction of the host with the guest molecule. The optimized distance between Cr and the S atom is 2.17 Å. The structure of the gas molecule after adsorption shows an increase in its bond length, and the value of the bond length after elongation is 1.45 Å. The sum of the radius of connected atoms is more than their bonding distance; thus, a strong type of interaction, *i.e.*, chemisorption, takes place.

The optimized structures of Sb_3MnO_6 with the SO_2 gas molecule adsorbed on the structure are shown in Fig. 10(e). The adsorption energy is −5.32 eV, which shows the good interaction of the host with the guest molecule. The optimized distance between Mn and the S atom is 2.61 Å. The structure of the gas molecule after adsorption shows an increase in its bond length, and the bond length after elongation is 1.54 Å. The sum of the radii of connected atoms is less than their bonding distance; thus, a weak type of interaction in the form of physisorption takes place. The optimized structures of Sb_3FeO_6 with the SO_2 gas molecule adsorbed on the structure are shown in Fig. 10(f). The value of adsorption energy is −5.09 eV, which shows the good interaction of the host with the guest molecule. The optimized distance between Fe and the O atom is 1.90 Å. The structure of the gas molecule after adsorption shows an increase in its bond length, and the bond length after elongation is 1.53 Å. The sum of the radii of connected atoms is greater than their bonding distance; thus, a strong chemisorption type of interaction takes place.

The optimized structures of Sb_3NiO_6 with the SO_2 gas molecule adsorbed on the structure are shown in Fig. 10(g). On the basis of the calculated adsorption energy of −4.45 eV, a strong interaction occurs. The optimized distance between the Ni and O atoms is 2.16 Å. The structure of the gas molecule after adsorption shows an increase in its bond length, and the bond length after elongation is 1.44 Å. The sum of the radii of connected atoms is less than their bonding distance; thus, a weak interaction, *i.e.*, physisorption, takes place. The optimized structures of Sb_3CoO_6 with the SO_2 gas molecule adsorbed on the structure are shown in Fig. 10(h). The value of the adsorption energy is −4.64 eV, which shows the good interaction of the host with the guest molecule. The optimized distance between Co and the O atom is 2.04 Å. The structure of the gas molecule after adsorption shows the increase in its bond length, and the bond length after elongation is 1.51 Å. The sum of the radii of connected atoms is less than their bonding distance; thus, a weak physisorption interaction takes place. The summary of the SO_2 gas adsorption is given in Table S4.

3.12. Electronic properties of the SO_2-adsorbed clusters

The calculated HOMO and LUMO energy values for Sb_3ScO_6–SO_2 are −6.86 and −5.55 eV, respectively, as shown in Fig. 11(a). The HOMO contributions from Sb, O and Sc are 48.4%, 1.37% and 44.44%, respectively. The LUMO contain 58.26% contribution from S and 1.22% from O. The Sb_3ScO_6 cluster exhibited η, S, μ, ΔE, and ω values of 0.65 eV, 1.52 eV^{-1}, −6.20 eV, 1.52 eV, and 29.38 eV, respectively. The hardness value is less than 2 eV, which indicates that the SO_2-adsorbed Sb_3ScO_6 is a soft material. For the SO_2-adsorbed Sb_3TiO_6 case, the computed HOMO and LUMO energies are −8.16 and −4.18 eV, respectively, as shown in Fig. 11(b). The contributions of Sb and O to the HOMO are 45.51% and 47.81%, respectively. The LUMO is composed of 36.22% Ti, 67.82% Sb and 3.33% O. The calculated η, S, μ, ΔE, and ω values for the Sb_3TiO_6 are 1.99 eV, 0.50 eV^{-1}, −6.17 eV, 0.50 eV and 9.57 eV, respectively. Since the hardness value is less than 2 eV, Sb_3TiO_6 has been identified as a soft material after the adsorption of SO_2. The calculated HOMO and LUMO energies for the Sb_3VO_6–SO_2 system are −5.34 and −3.15 eV, respectively, as shown in Fig. 11(c). The HOMO has −5.75% and 22.95% contributions from S and V, respectively. The LUMO has 59.12% contribution from V, 9.64% from Sb and 8.4% from O.

The Sb_3VO_6 cluster demonstrated calculated η, S, μ, ΔE, and ω values of 1.09 eV, 0.91 eV^{-1}, −4.24 eV, 0.91 eV, and 8.23 eV, respectively. The hardness value is less than 2 eV, which indicates that Sb_3VO_6 adsorbed by the SO_2 gas molecule is a soft material. For Sb_3CrO_6–SO_2, the computed HOMO and LUMO energies are −6.33 and −5.12 eV, respectively, as shown in Fig. 11(d). The contributions of Cr, S and O to the HOMO are 50.2%, 6.02% and 30.5%, respectively. The LUMO is composed of 2.43% antimony, 66.73% chromium and 9.72% oxygen. The calculated η, S, μ, ΔE, and ω values for the SO_2-adsorbed Sb_3CrO_6 are 0.60 eV, 1.65 eV^{-1}, −5.72 eV, 1.65 eV and 27.09 eV, respectively. Since the hardness value is less than 2 eV, Sb_3CrO_6 has been identified as a soft material. The calculated HOMO and LUMO energies for Sb_3MnO_6–CO_2 are −6.79 and −3.66 eV, respectively, as shown in Fig. 11(e). The HOMO contributions from Sb, Mn and O are 2.49%, 64.01% and 23.05%, respectively. The LUMO contains 58.41% contribution from Mn, 1.35% from Sb, and O from 29.23%. The Sb_3ScO_6 cluster exhibited η, S, μ, ΔE, and ω values of 1.56 eV, 0.63 eV^{-1}, −5.22 eV, 0.63 eV, and −8.73 eV, respectively. The hardness value is less than 2 eV, which indicates that the CO_2-adsorbed Sb_3MnO_6 is a soft material. For the Sb_3FeO_6–SO_2 case, the computed HOMO and LUMO energies are −6.56 and −5.40 eV, respectively, as shown in Fig. 11(f). The contributions of S and O to the HOMO are 3.6%, and 27.15%, respectively. The LUMO is composed of 52.51% S and 47.11% O. The calculated η, S, μ, ΔE, and ω values for the Sb_3FeO_6 are 0.58 eV, 1.72 eV^{-1}, −5.98 eV, 1.72 eV and 30.86 eV, respectively. Since the hardness value is larger than 2 eV, the Sb_3FeO_6 cluster is identified as a hard material.

The calculated HOMO and LUMO energies for the SO_2-adsorbed Sb_3NiO_6 are −7.19 and −3.73 eV, respectively, as

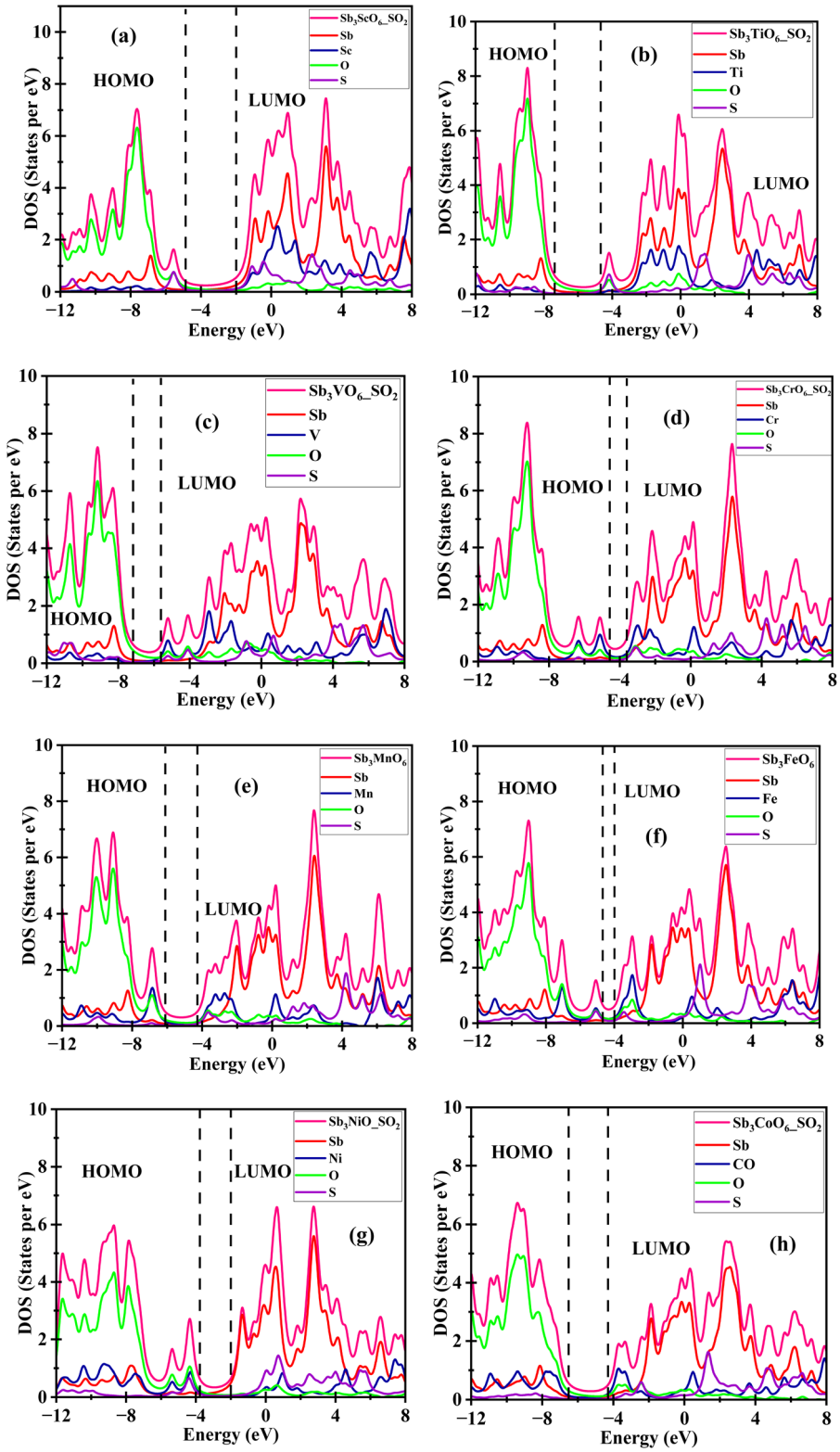

Fig. 11 Calculated electronic properties of SO_2-adsorbed $Sb_3(TM)O_6$ (where TM is Sc, Ti, V, Cr, Mn, Fe, Ni, and Co): (a) Sb_3ScO_6, (b) Sb_3TiO_6, (c) Sb_3VO_6, (d) Sb_3CrO_6, (e) Sb_3MnO_6, (f) Sb_3FeO_6, (g) Sb_3NiO_6, and (h) Sb_3CoO_6.

shown in Fig. 11(g). The HOMO contributions of Ni, Sb and O are 29.63%, 11.71% and 48.36%. The LUMO contain 10.26% contribution from Ni, 47.57% from S and 36.86% from O. The Sb_3NiO_6 exhibited η, S, μ, ΔE, and ω values of 1.03 eV, 0.96 eV^{-1}, −6.54 eV, 0.96 eV, and 21 eV, respectively. The hardness value is less than 2 eV, which indicates that the SO_2-adsorbed Sb_3NiO_6 is

a soft material. For Sb_3CoO_6, the computed HOMO and LUMO energies are −7.19 and −3.73 eV, respectively, as shown in Fig. 11(h). The contributions of Sb, Co, and O to the HOMO are 4.28%, 39.89% and 49.66%, respectively. The LUMO is composed of 65.67% Co, 2.89% Sb and 23.29% O. The calculated values for the Sb_3CoO_6 are 1.73 eV, 0.58 eV^{-1}, −5.46 eV, 0.58 eV, and 8.62 eV for η, S, μ, ΔE, and ω, respectively. Since the hardness value is less than 2 eV, Sb_3CoO_6 has been identified as a soft material.

3.13. Charge transfer integral (CTI) of the SO_2 adsorbed clusters

As discussed above, the charge transfer integral for Sb_3ScO_6 is calculated, which yields electron- and hole-transfer energies of 0.02 and 0.01 eV, respectively, as well as a recombination energy of 0.62 eV from fragment 1 to fragment 2. Conversely, the recombination energy from fragment 2 to 1 is 0.01 eV, as shown in Fig. 12(a). For Sb_3TiO_6, the calculated electron- and hole-transfer energies are 0.46 and 1.69 eV, respectively, and the recombination energy from fragment 1 to fragment 2 is 0.34 eV, while the recombination energy from fragment 2 to 1 is 0.08 eV, as shown in Fig. 12(b). For Sb_3VO_6, the calculated electron- and hole-transfer energies are 0.45 and 0.03 eV, respectively, and the recombination energy from fragment 1 to fragment 2 is 0.72 eV, while the recombination energy from fragment 2 to 1 is 0.12 eV, as shown in Fig. 12(c). For Sb_3CrO_6, the calculated electron- and hole-transfer energies are 0.57 and 1.57 eV, respectively, and the recombination energy from fragment 1 to fragment 2 is 0.11 eV, while the recombination energy from fragment 2 to 1 is 0.07 eV, as shown in Fig. 12(d). For Sb_3MnO_6, the calculated electron- and hole-transfer energies are 0.64 and 0.19 eV, respectively, and the recombination energy from fragment 1 to fragment 2 is 0.09 eV, while the recombination energy from fragment 2 to 1 is 0.23 eV, as shown in Fig. 12(e). For Sb_3FeO_6, the calculated electron- and hole-transfer energies are 0.44 and 0.36 eV, respectively, and the recombination energy from fragment 1 to fragment 2 is 0.30 eV, while the recombination energy from fragment 2 to 1 is 0.10 eV. For Sb_3CoO_6, the calculated electron- and hole-transfer energies are 0.20 and 0.06 eV, respectively, and the recombination energy from fragment 1 to fragment is 2 0.05 eV, while the recombination energy from fragment 2 to 1 is 0.69 eV, as shown in Fig. 12(f). For Sb_3NiO_6, the calculated electron- and hole-transfer energies are 0.45 and 0.03 eV, respectively, and the recombination energy from fragment 1 to fragment 2 is 0.72 eV, while the recombination energy from fragment 2 to 1 is 0.12 eV, as shown in Fig. 12(g). For Sb_3CoO_6, the calculated electron- and hole-transfer energies are 0.04 and 0.53 eV, respectively, and the recombination energy from fragment 1 to fragment 2 is 0.09 eV, while the recombination energy from fragment 2 to 1 is 0.31 eV, as shown in Fig. 12(h).

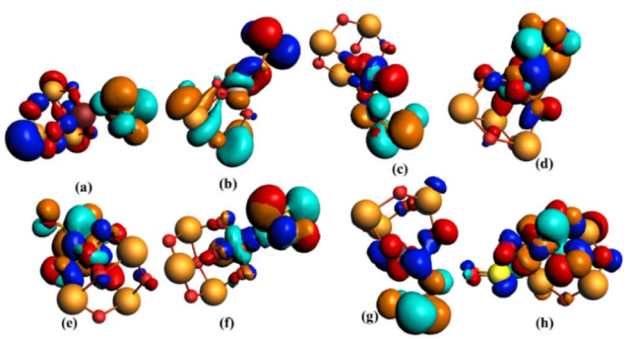

Fig. 12 Charge transfer integral calculations for Sb_3TMO_6 as HOMO–LUMO: (a) Sb_3ScO_6, (b) Sb_3TiO_6, (c) Sb_3VO_6, (d) Sb_3CrO_6, (e) Sb_3MnO_6, (f) Sb_3FeO_6, (g) Sb_3NiO_6 and (h) Sb_3CoO_6.

3.14. Stability of the fully loaded structure of SO_2

The stability levels of the SO_2-absorbed Sb_3ScO_6, Sb_3TiO_6, Sb_3VO_6, Sb_3CrO_6, Sb_3MnO_6, Sb_3FeO_6, Sb_3NiO_6 and Sb_3CoO_6 are represented in Fig. 13, which shows a snapshot of cages after absorption and the change in energy and temperature over the time interval. AIMD simulations were carried out at a high temperature of 600 K.

The AIMD simulation carried out in the case of the SO_2-adsorbed Sb_3TMO_6 structure yields plots of temperature and energy against time, as illustrated in Fig. 13. The energy of all systems remained rather constant over the simulations or moved towards final equilibrium positions, showing the stability of the structure after the absorption of gas molecules. The snapshots of the structures are also displayed in Fig. 13 to showcase that there is no structural change after the absorption. The structural study shows that there is no bond breakage, indicating the stability of the materials.

3.15. Adsorption of NH_3

The optimized structures of Sb_3ScO_6 with an NH_3 gas molecule adsorbed on the structure are shown in Fig. 14(a). The adsorption energy is −1.59 eV, which shows the good interaction of the host with the guest molecule. The optimized distance between Sc and the N atom is 2.36 Å. The structure of the gas molecule after adsorption shows a decrease in the bond length, and the bond length after shortening is 1.01 Å. The sum of the radii of the connected atoms is less than their bonding distance; thus, a weak type of interaction, *i.e.*, physisorption, takes place. The optimized structures of Sb_3TiO_6 with the NH_3 gas molecule adsorbed on its structure are shown in Fig. 14(b). The adsorption energy is −0.70 eV, which shows the good interaction of the host with the guest molecule. The optimized distance between Ti and the N atom is 2.26 Å. The structure of the gas molecule after adsorption shows a decrease in its bond length, and the bond length after shortening is 1.01 Å. The sum of the radii of connected atoms is less than their bonding distance; thus, a weak type of interaction, *i.e.*, physisorption, takes place. The optimized structures of Sb_3VO_6 with an NH_3 gas molecule adsorbed on the structures are shown in Fig. 14(c), which points to an adsorption energy of −0.02 eV and a large vertical distance of 4.41 Å. These results show a very weak physisorption interaction between the host and CO. The optimized structures of Sb_3CrO_6 with an NH_3 gas molecule adsorbed on the structure are shown in Fig. 14(d). The adsorption energy is −0.92 eV, which shows the good interaction of the host

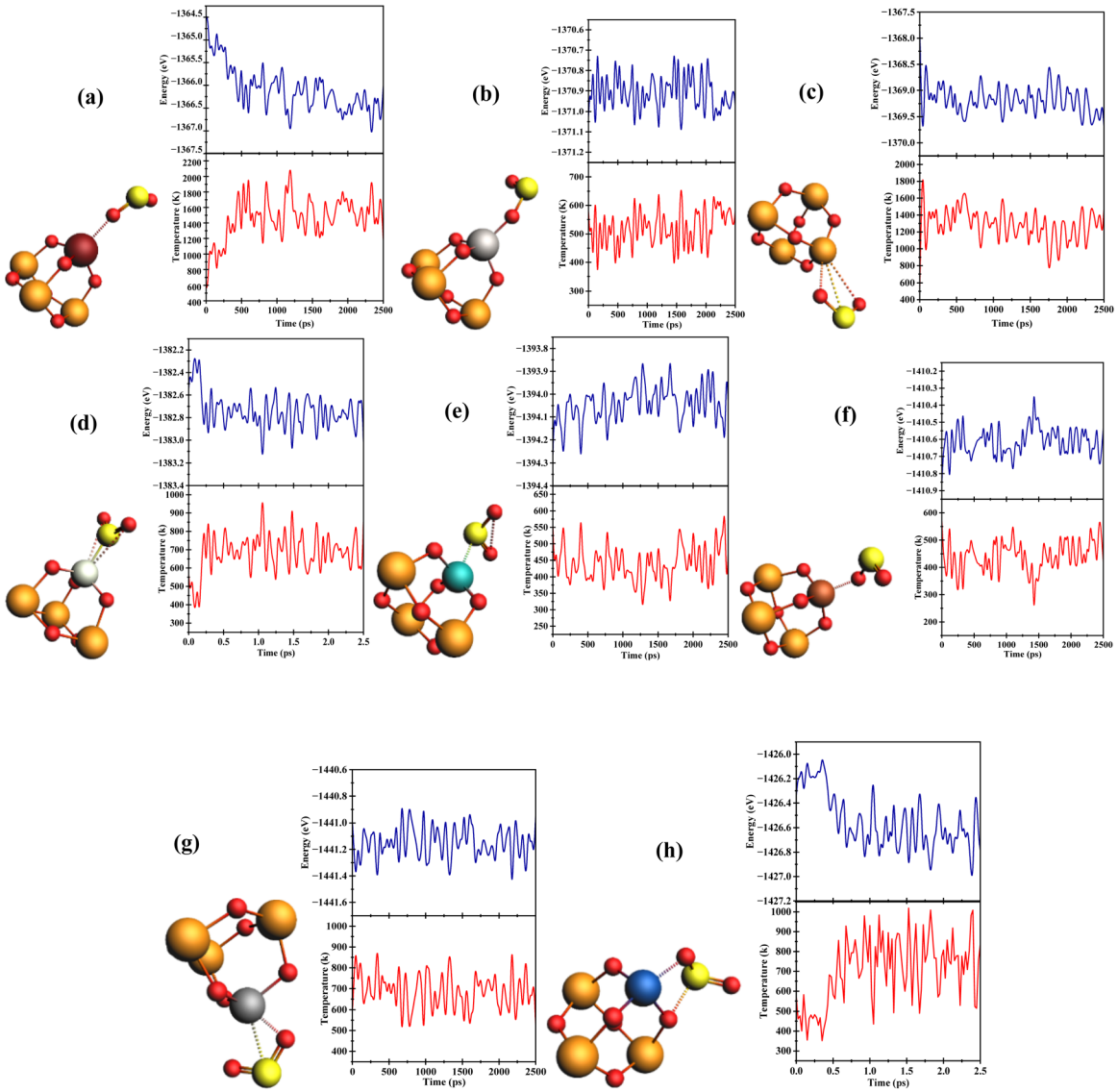

Fig. 13 AIMD simulation of the fully loaded SO_2-absorbed (a) Sb_3ScO_6, (b) Sb_3TiO_6, (c) Sb_3VO_6, (d) Sb_3CrO_6, (e) Sb_3MnO_6, (f) Sb_3FeO_6, (g) Sb_3NiO_6 and (h) Sb_3CoO_6.

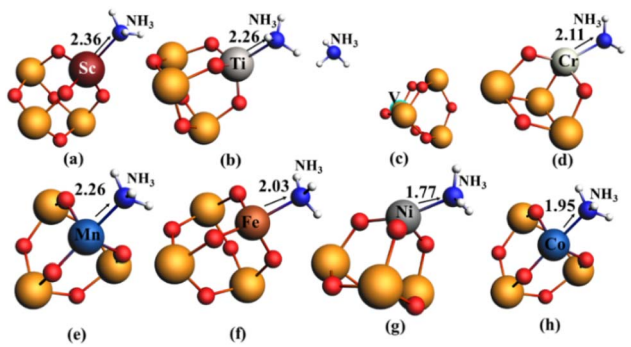

Fig. 14 Optimized structures of the SO_2-gas-adsorbed clusters of (a) Sb_3SCO_6, (b) Sb_3TiO_6, (c) Sb_3VO_6, (d) Sb_3CrO_6, (e) Sb_3MnO_6, (f) Sb_3FeO_6, (g) Sb_3NiO_6 and (h) Sb_3CoO_6.

with the guest molecule. The optimized distance between Cr and the N atom is 2.11 Å. The structure of the gas molecule after adsorption shows a decrease in its bond length, and the bond length after shortening is 1.01 Å. The sum of the radii of the connected atoms is 1.95 Å, which is less than their bonding distance; thus, the weak physisorption interaction takes place.

The optimized structures of Sb_3MnO_6 with an NH_3 gas molecule adsorbed on the structure are shown in Fig. 14(e). The value of the adsorption energy highlights the good interaction of the host with the guest molecule. The optimized distance between Mn and the N atom is 2.26 Å. The structure of the gas molecule after adsorption shows an increase in the bond length, and the bond length after the elongation is 1.08 Å. The sum of the radius of the connected atom is 1.99 Å, which is less than their bonding distance; thus, a weak type of interaction, *i.e.*, physisorption, takes place. The optimized structures of

Sb_3FeO_6 with an NH_3 gas molecule adsorbed on the structure are shown in Fig. 14(f). The value of adsorption energy is −1.03 eV, which shows the good interaction of the host with the guest molecule. The optimized distance between Fe and the N atom is 2.36 Å. The sum of the radius of the connected atom is 2.03 Å, which is less than their bonding distance, pointing to weak physisorption.

The optimized structures of Sb_3NiO_6 with an NH_3 gas molecule adsorbed on the structure are shown in Fig. 14(g). The adsorption energy is −0.55 eV, which shows the good interaction of the host with the guest molecule. The optimized distance between the Ni and N atom is 1.77 Å. The structure of the gas molecule after adsorption shows a decrease in its bond length, and the value of the bond length after shortening is 1.01 Å. The sum of the radii of connected atoms is greater than their bonding distance; thus, a strong type of interaction, which is also known as chemisorption, takes place. The optimized structures of Sb_3ScO_6 with an NH_3 gas molecule adsorbed on the structure are shown in Fig. 14(h). The value of adsorption energy is −0.54 eV, which shows the good interaction of the host with the guest molecule. The optimized distance between Co and the N atom is 1.95 Å. The structure of the gas molecule after adsorption shows a decrease in its bond length, and the value of the bond length after shortening is 1.01 Å. The sum of the radii of connected atoms is greater than their bonding distance; thus, a strong chemisorption interaction takes place. The summary of results on NH_3 gas adsorption is mentioned in Table S5.

3.16. Electronic properties of the NH_3-adsorbed clusters

The calculated HOMO and LUMO energies for the Sb_3ScO_6–NH_3 system are −6.80 and −1.44 eV, respectively, as shown in Fig. 15(a). The HOMO contributions from Sb, Sc and O are 47.91%, 2.84% and 44.82%, respectively. The LUMO contains 91.25% H, 1.76% N and 8.76% Sc. The calculated values of η, S, μ, ΔE, and ω for the Sb_3ScO_6 cluster are 2.68 eV, 0.37 eV^{-1}, 04.12 eV, 0.37 eV, and 4.37 eV, respectively. The hardness value is greater than 2 eV, which indicates that the NH_3-adsorbed Sb_3ScO_6 is a soft material.

For the Sb_3TiO_6–NH_3 system, the computed HOMO and LUMO energies are −7.25 and −2.41 eV, respectively, as shown in Fig. 15(b). The contributions of Sb and O to the HOMO are 48.18 and 43.08%, respectively. The LUMO is composed of 19.7% Ti, 74.09% Sb and 0.46% O. The calculated η, S, μ, ΔE, and ω values for the Sb_3TiO_6 are 2.42 eV, 0.41 eV, −4.83 eV, 0.41 eV and 4.82 eV, respectively. Since the hardness value is greater than 2 eV, the NH_3-adsorbed Sb_3TiO_6 has been identified as a hard material. The calculated HOMO and LUMO energies for the Sb_3VO_6–NH_3 system are −5.16 and −2.0 eV, respectively, as shown in Fig. 15(c). The HOMO has 2.36% and 92.45% contributions from O and V, respectively. The LUMO has 62.7% contribution from V, 27.15% from Sb and 1.45% from O. The Sb_3VO_6 cluster exhibits values of 1.58 eV, 0.63 eV^{-1}, −3.58 eV, 0.63 eV, and 4.06 eV, respectively. The hardness value is less than 2 eV, which indicates that the NH_3-adsorbed Sb_3VO_6 is a soft material. For the Sb_3CrO_6–NH_3 system, the computed HOMO and LUMO energies are −4.81 and −3.38 eV, respectively, as shown in Fig. 15(d). The contributions of Cr and O to the HOMO are 80.59 and 11.29%, respectively. The LUMO is composed of 89.47% Sb, 1.44% Cr and O 3.83%. The calculated η, S, μ, ΔE, and ω values for the SO_2-adsorbed Sb_3CrO_6 are 0.71 eV, 1.40 eV^{-1}, −4.09 eV, 1.40 eV and 11.73 eV, respectively. Since the hardness value is less than 2 eV, Sb_3CrO_6 is identified as a soft material.

The calculated HOMO and LUMO energies for Sb_3MnO_6–NH_3 are −4.63 and −1.97 eV, respectively, as shown in Fig. 15(e). The HOMO contributions from H, Mn and O are 13.06%, 88.47% and 1.74%, respectively. The LUMO contains 58.41% contribution from Mn, 82.34% from Sb and 9.23% from O. The Sb_3ScO_6 cluster exhibited η, S, μ, ΔE, and ω values of 1.33 eV, 0.75 eV^{-1}, −3.30 eV, 0.75, 4.09 eV, respectively. The hardness value is less than 2 eV, which indicates that the NH_3-adsorbed Sb_3MnO_6 is a soft material. For Sb_3FeO_6–SO_2, the computed HOMO and LUMO energies are −6.21 and −4.41 eV, respectively, as shown in Fig. 15(f). The contributions of Sb, Fe, and O to the HOMO are 1.44, 51.4, and 28.73%, respectively. The LUMO is composed of 7.73% Sb and 41.11% oxygen. The calculated η, S, μ, ΔE, and ω values for the Sb_3FeO_6 are 0.90 eV, 1.11 eV^{-1}, −5.31 eV, 1.11 eV, and 15.66 eV, respectively. Since the hardness value is less than 2 eV, the NH_3-adsorbed Sb_3FeO_6 cluster has been identified as a soft material. The calculated HOMO and LUMO energies for the NH_3-adsorbed Sb_3NiO_6 are −6.71 and −2.61 eV, respectively, as shown in Fig. 15(g). The HOMO contributions from Ni, Sb, and O are 3.86, 10.68, and 72.89%, respectively. The LUMO contains 7.4% Ni, 61.4% Sb, and 12.36% oxygen. The values of η, S, μ, ΔE, and ω calculated for Sb_3NiO_6 are 2.05 eV, 0.49 eV^{-1}, −4.66 eV, 0.49 eV, and 5.30 eV, respectively. The hardness value is greater than 2 eV, which indicates that the NH_3-adsorbed Sb_3NiO_6 is a hard material. For Sb_3CoO_6–NH_3, the computed HOMO and LUMO energies are −6.39 and −2.84 eV, respectively, as shown in Fig. 15(h). The contributions of Sb, Co, and O to the HOMO are 8.38, 40.63 and 43.56%, respectively. The LUMO is composed of 66.05% Co, 3.35% Sb and 27.17% O. The calculated values of η, S, μ, ΔE, and ω for the Sb_3CoO_6 cluster are 1.77 eV, 0.56 eV^{-1}, −4.61 eV, 0.56 eV and 6 eV, respectively. Since the hardness value is less than 2 eV, the NH_3-adsorbed Sb_3CoO_6 cluster has been identified as a soft material.

3.17. Charge transfer integral (CTI) of the NH_3-adsorbed clusters

As discussed above, for the Sb_3ScO_6, the CTI-calculated electron- and hole-transfer energies are 0.10 and 0.06 eV, respectively, and the recombination energy from fragment 1 to fragment 2 is 0.91 eV, while the recombination energy from fragment 2 to 1 is 0.05 eV, as shown in Fig. 16(a). For Sb_3TiO_6, the calculated electron- and hole-transfer energies are 0.22 and 1.64 eV, respectively, and the recombination energy from fragment 1 to fragment 2 is 0.78 eV, while the recombination energy from fragment 2 to 1 is 0.22 eV, as represented in Fig. 16(b). For Sb_3CrO_6, the calculated electron- and hole-transfer energies are 0.25 and 1.02 eV, respectively, and the recombination energy from fragment 1 to fragment 2 is 0.25 eV, while the

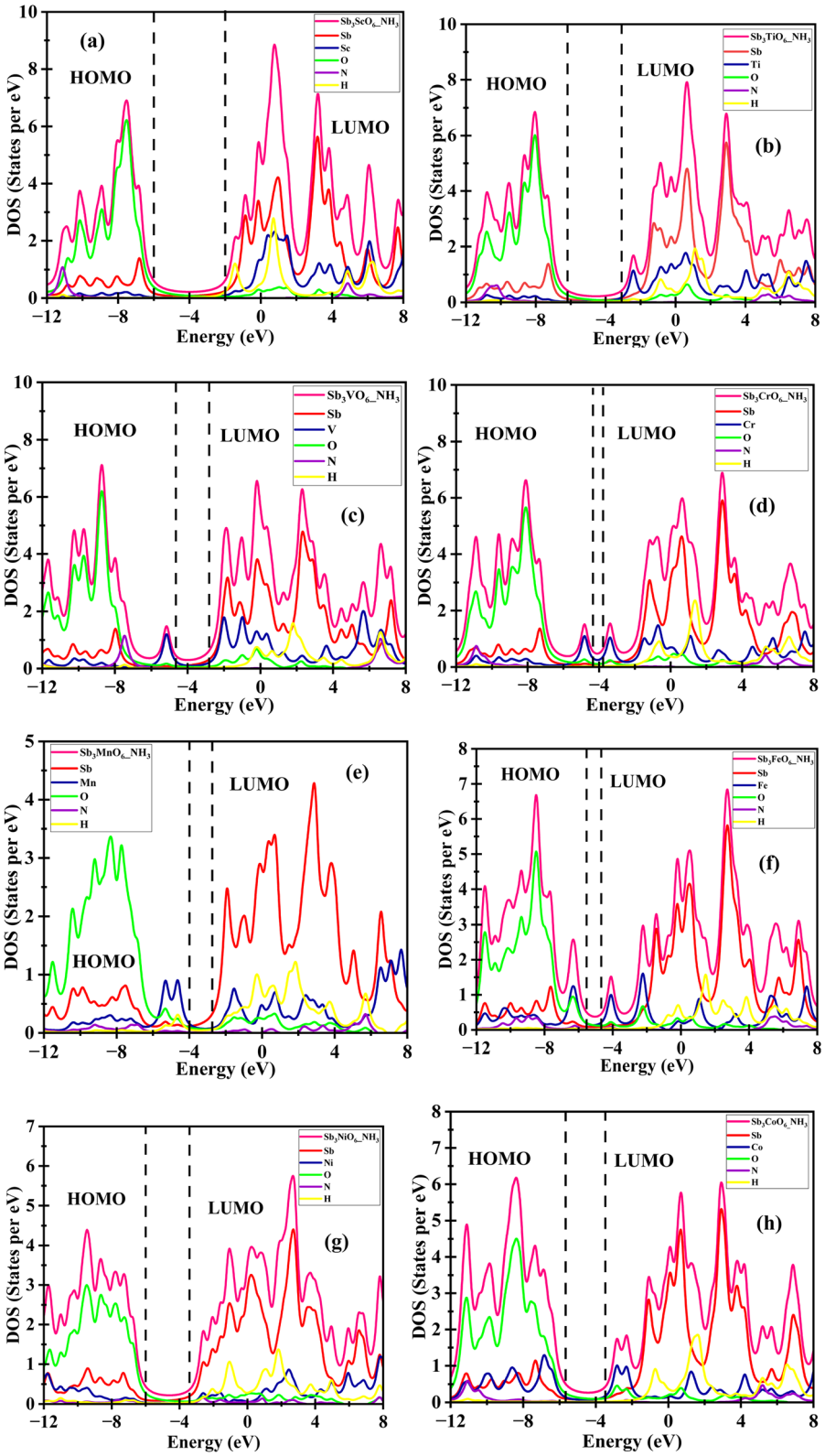

Fig. 15 Calculated electronic properties of the NH_3-adsorbed $Sb_3(TM)O_6$ (where TM is Sc, Ti, V, Cr, Mn, Fe, Ni, and Co): (a) Sb_3ScO_6, (b) Sb_3TiO_6, (c) Sb_3VO_6, (d) Sb_3CrO_6, (e) Sb_3MnO_6, (f) Sb_3FeO_6, (g) Sb_3NiO_6, and (h) Sb_3CoO_6.

recombination energy from fragment 2 to 1 is 0.08 eV, as shown in Fig. 16(c). For Sb_3MnO_6, the calculated electron- and hole-transfer energies are 1.13 and 0.33 eV, respectively, and the recombination energy from fragment 1 to fragment 2 is 2.45 eV, while the recombination energy from fragment 2 to 1 is 1.15 eV, as represented in Fig. 16(d). For Sb_3FeO_6, the calculated

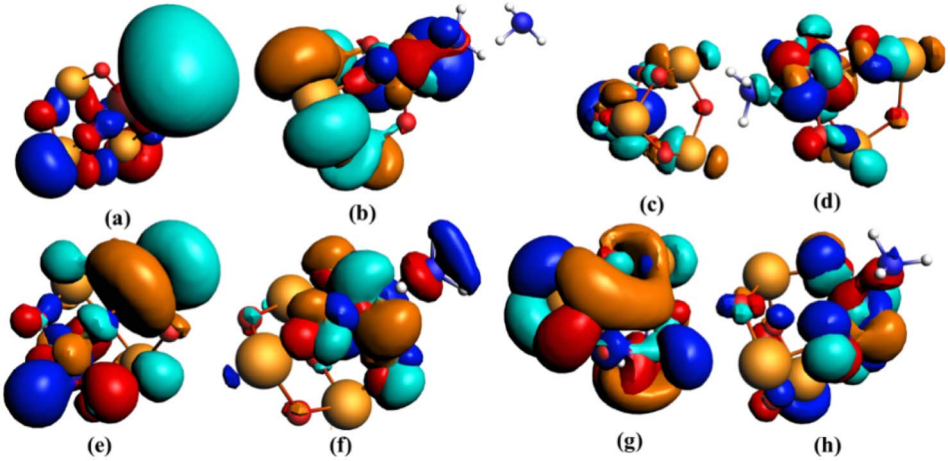

Fig. 16 Charge transfer integral calculations for Sb_3TMO_6 as HOMO–LUMO: (a) Sb_3ScO_6, (b) Sb_3TiO_6, (c) Sb_3VO_6, (d) Sb_3CrO_6, (e) Sb_3MnO_6, (f) Sb_3FeO_6, (g) Sb_3NiO_6 and (h) Sb_3CoO_6.

electron- and hole-transfer energies are 0.44 and 0.17 eV, respectively, and the recombination energy from fragment 1 to fragment 2 is 0.42 eV, while the recombination energy from fragment 2 to 1 is 0.07 eV, as shown in Fig. 16(e). For Sb_3CoO_6, the calculated electron- and hole-transfer energies are 0.02 and 0.66 eV, respectively, and the recombination energy from fragment 1 to fragment 2 is 0.05 eV, while the recombination energy from fragment 2 to 1 is 0.12 eV, as shown in Fig. 16(f). For Sb_3NiO_6, the calculated electron- and hole-transfer energies are 0.45 and 0.03 eV, respectively, and the recombination energy from fragment 1 to fragment 2 is 0.72 eV, while the recombination energy from fragment 2 to 1 is 0.12 eV, as shown in Fig. 16(g). For Sb_3CoO_6, the calculated electron- and hole-transfer energies are 1.16 and 1.34 eV, respectively, and the recombination energy from fragment 1 to fragment 2 is 1.44 eV, while the recombination energy from fragment 2 to 1 is 1.38 eV, as represented in Fig. 16(h).

3.18. Stability of the loaded structure of NH_3-adsorbed Sb_3TMO_6

The stability of the NH_3-absorbed Sb_3ScO_6, Sb_3TiO_6, Sb_3CrO_6, Sb_3MnO_6, Sb_3FeO_6, and Sb_3CoO_6 is represented in Fig. 17, which also gives a snapshot after absorption and the change in

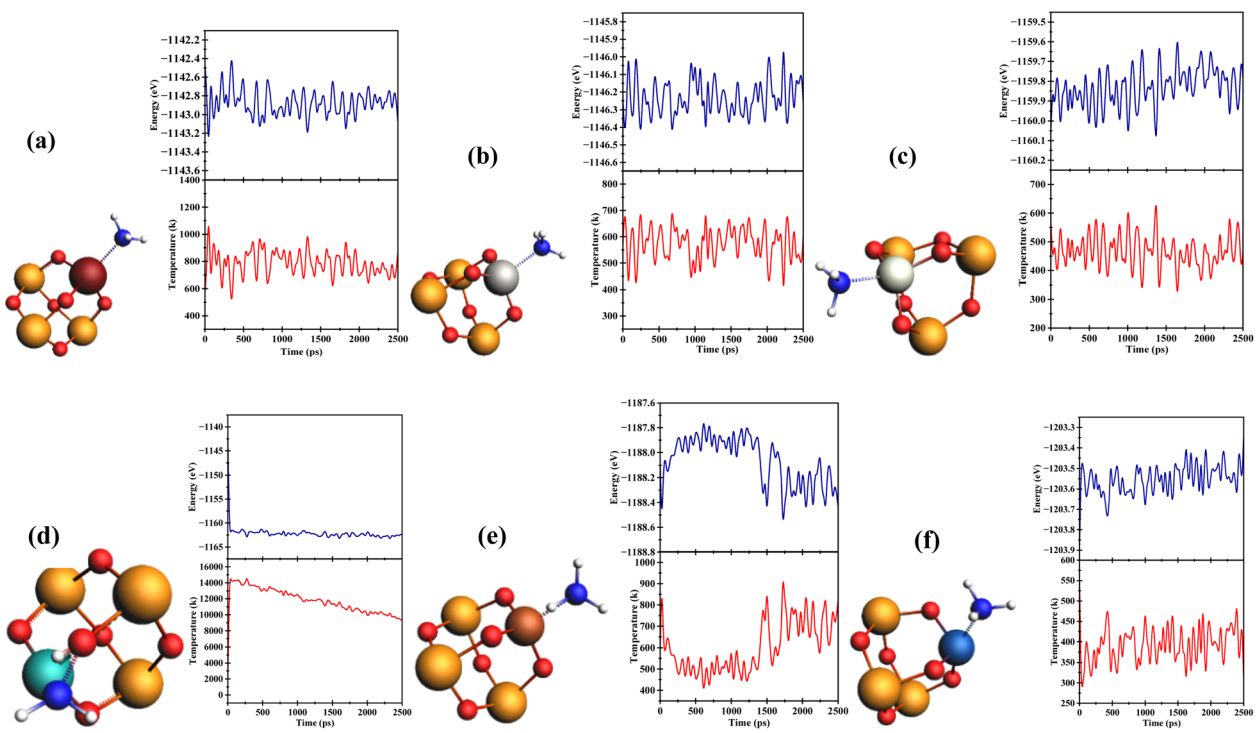

Fig. 17 AIMD simulations of the fully loaded NH_3-absorbed (a) Sb_3ScO_6, (b) Sb_3TiO_6, (c) Sb_3CrO_6, (d) Sb_3MnO_6, (e) Sb_3FeO_6 and (f) Sb_3CoO_6.

energy and temperature over the time interval. The energy of all systems remained rather constant over the simulations, as shown in Fig. 17(a), (b), (c), (d), (e) and (f), respectively. The structural study shows that there is no bond breakage, indicating the stability of the materials.

3.19. Adsorption of CH_4

The optimized structures of Sb_3ScO_6 with a CH_4 gas molecule adsorbed on the structure are shown in Fig. 18(a). The adsorption energy is −6.23 eV, which shows the good interaction of the host with the guest molecule. The optimized distance between Sc and the C atom is 2.48 Å. The structure of the gas molecule after adsorption shows an increase in its bond length, and the value of the bond length after elongation is 1.46 Å.

The sum of the radii of connected atoms is less than their bonding distance; thus, a weak physisorption type of interaction takes place. The optimized structures of Sb_3TiO_6 and Sb_3VO_6, with a CH_4 gas molecule adsorbed on the structures, are shown in Fig. 18(b) and (c). The adsorbed energies are low in this case, *i.e.*, −1.04 and −1.096 eV, whereas large vertical distances of 4.13 and 4.02 Å are observed. The results show a very weak physisorption interaction between the host and guest molecule, indicating the absence of any change in the structure of the host.

The optimized structures of Sb_3CrO_6 with a CH_4 gas molecule adsorbed on the structure are shown in Fig. 18(d). The value of the adsorption energy is −2.67 eV, which indicates the good interaction of the host with the guest molecule. The optimized distance between Cr and the C atom is 2.04 Å. The structure of the gas molecule after adsorption shows an increase in its bond length, and the value of the bond length after elongation is 1.45 Å. The sum of the radius of the connected atom is 2.03 Å, which is less than their bonding distance, pointing to physisorption. The optimized structures of Sb_3MnO_6 with the CH_4 gas molecule adsorbed on the structure are shown in Fig. 18(e). The adsorption energy is −5.88 eV, which shows the good interaction of the host with the guest molecule. The optimized distance between Mn and the C atom is 2.40 Å. The structure of the gas molecule after adsorption shows an increase in its bond length, and the bond length after elongation is 1.54 Å. The sum of the radii of the connected atoms is 2.06 Å, which is less than their bonding distance; thus, a weak physisorption interaction takes place.

The optimized structures of Sb_3FeO_6, Sb_3NiO_6, and Sb_3CoO_6 with the CH_4 gas molecule adsorbed on the structure are shown in Fig. 18(f), (g) and (h), respectively. The adsorbed energies are −1.97, −0.51 and −0.90 eV. The vertical distances are large, with values of 4.38, 4.10 and 4.09 Å, pointing to a very weak interaction between the host and the guest molecule. The adsorption in this case is physisorption, and it produces no change in the structure of the host. The structural properties of the CH_4-absorbed Sb_3TMO_6 are described in Table S6.

The computed adsorption energies demonstrate that the $Sb_3(TM)O_6$ clusters display significant TM-dependent modifications in gas interactions, providing good selectivity at room temperature. CH_4 interacts poorly with all TM sites ($E_a \approx -0.5$ eV, physisorption), but gases such as SO_2 and NH_3 show substantially greater adsorption (up to −6.32 eV for SO_2 on Sb_3TiO_6). This considerable variation in binding strength means that under ambient settings, the sensors preferentially adsorb and respond to strongly interacting gases, while weakly adsorbing molecules, such as CH_4, generate minimal interference, ensuring good discrimination at room temperature. As compared to conventional TM-doped metal-oxide sensors, $Sb_3(TM)O_4$ cage materials have the potential to demonstrate good sensing performance, with high sensitivity and selectivity. The adsorption experiments demonstrate that gas–host interactions are strongly dependent on the TM site, enabling selective detection. With the exception of Sb_3ScO_4 ($E_a = -0.81$ eV), CO_2 interacts weakly with a majority of TM sites ($E_a < -0.5$ eV), SO_2 exhibits significant chemisorption on V and Cr sites, and NH_3 adsorption varies from physisorption to chemisorption depending on the TM. High adsorption energies (*e.g.*, −5.49 eV to −6.32 eV for SO_2) demonstrate significant charge transfer, which may enhance the sensor sensitivity, although even the physisorption scenario creates noticeable structural disturbances. Similarly, NH_3 adsorption fluctuates from physisorption to chemisorption depending on the TM, indicating flexible modification of selectivity based on the TM choice. High adsorption energies (*e.g.*, −5.49 eV and −6.32 eV for some SO_2 and $Sb_3(TM)O_4$ interactions) indicate significant charge transfer upon binding, which would probably result in significant changes in the electronic characteristics and great sensitivity in a practical sensor. Even physisorption with CO_2 or CH_4 causes noticeable structural perturbations (bond elongation), showing that even weakly interacting gases can stimulate a meaningful sensor response.

In contrast, ordinary TM-doped metal-oxide sensors frequently display low selectivity need high working temperatures while suffering from environmental sensitivity. Reversible physisorption and strong chemisorption are made possible by the adjustable TM-dependent adsorption on $Sb_3(TM)O_4$. This dual-mode mechanism offers excellent sensitivity, selectivity and possibly lower power operation, which is a distinct benefit over previously reported TM-doped sensors.

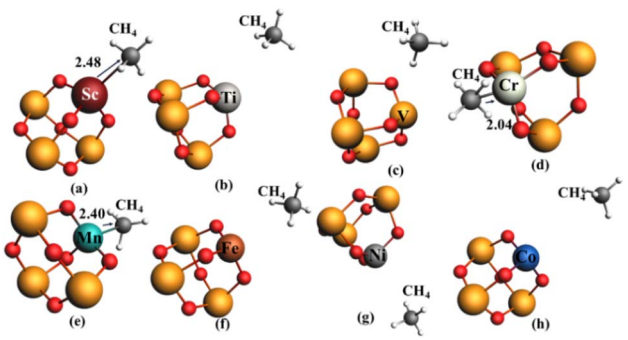

Fig. 18 Optimized structures of the CH_4-gas-adsorbed (a) Sb_3ScO_6, (b) Sb_3TiO_6, (c) Sb_3VO_6, (d) Sb_3CrO_6, (e) Sb_3MnO_6, (f) Sb_3FeO_6, (g) Sb_3NiO_6 and (h) Sb_3CoO_6.

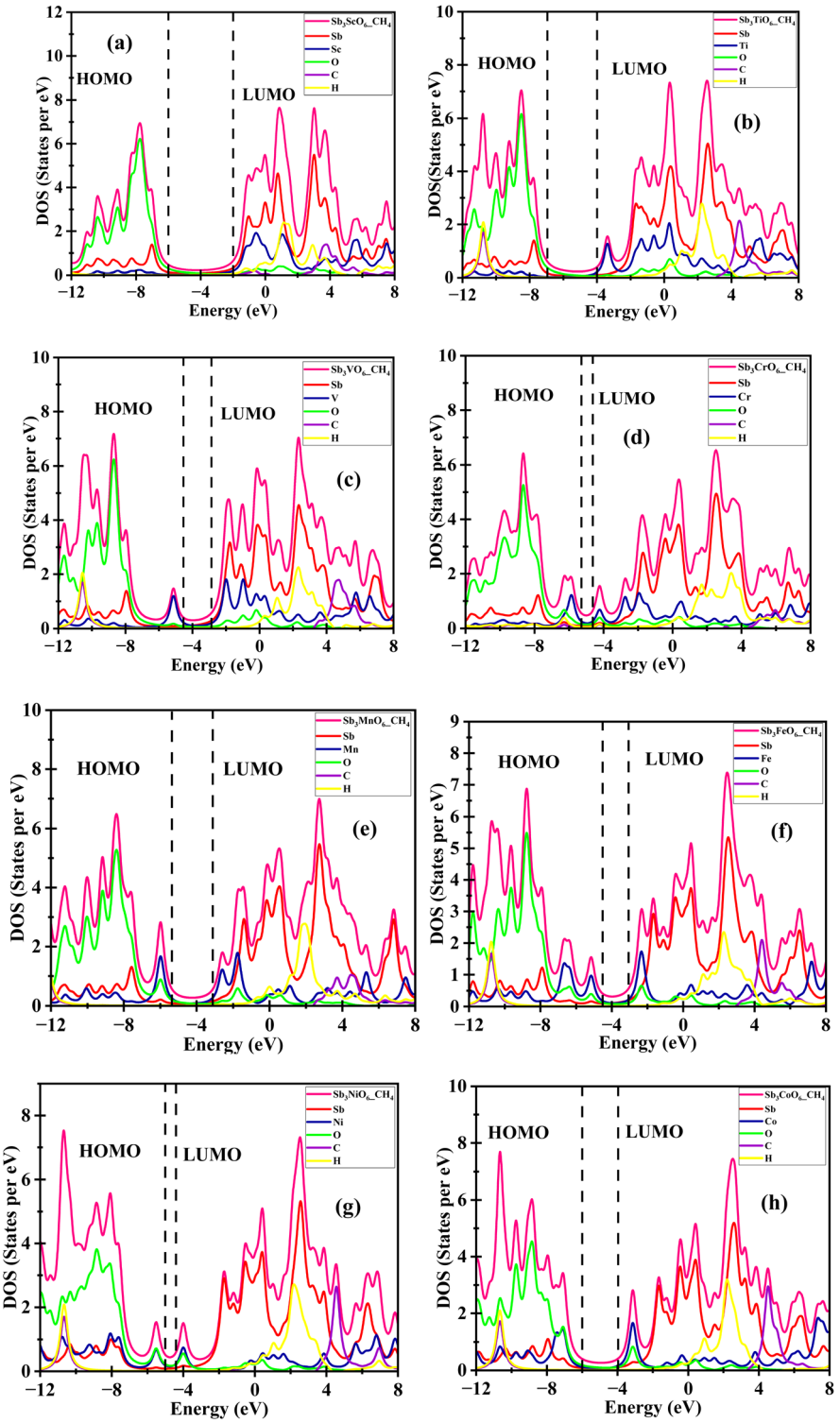

Fig. 19 Calculated electronic properties of the CH_4-adsorbed $Sb_3(TM)O_6$ (where TM is Sc, Ti, V, Cr, Mn, Fe, Ni, and Co): (a) Sb_3ScO_6, (b) Sb_3TiO_6, (c) Sb_3VO_6, (d) Sb_3CrO_6, (e) Sb_3MnO_6, (f) Sb_3FeO_6, (g) Sb_3NiO_6, and (h) Sb_3CoO_6.

3.20. Electronic properties of the CH_4-adsorbed clusters

The calculated HOMO and LUMO energies for Sb_3ScO_6–CH_4 are −7.04 and −1.11 eV, respectively, as shown in Fig. 19(a). The HOMO contributions from Sb, Sc, and O are 45.5, 2.10, and 40.03%, respectively. The LUMO contains 9.26% contribution from Sc and 80.99% from Sb. The Sb_3ScO_6 cluster exhibits η, S, μ, ΔE, and ω values of 2.96 eV, 0.33 eV^{-1}, 0.35 eV, −4.07 eV, and 2.80 eV, respectively. The hardness value is greater than 2 eV, which indicates that the CH_4-adsorbed Sb_3ScO_6 is a hard

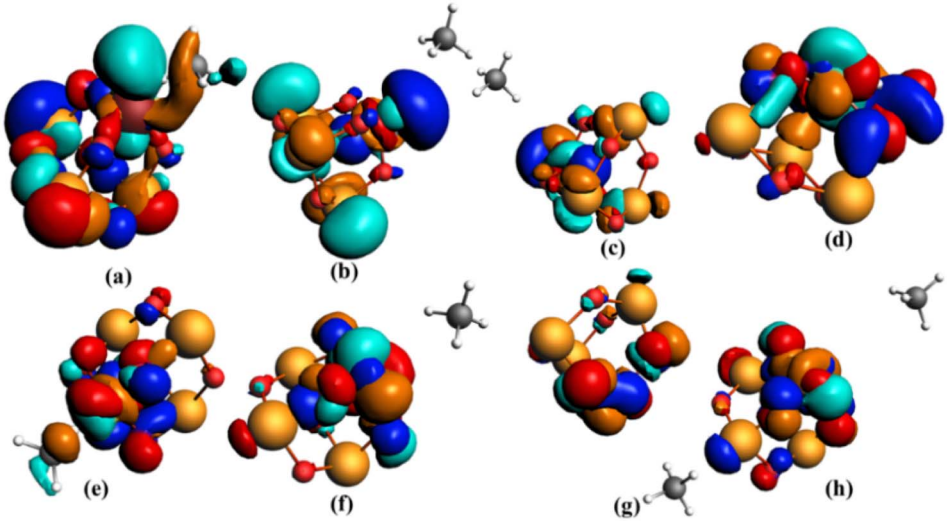

Fig. 20 Charge transfer integral calculations on Sb_3TMO_6 as HOMO–LUMO: (a) Sb_3ScO_6, (b) Sb_3TiO_6, (c) Sb_3VO_6, (d) Sb_3CrO_6, (e) Sb_3MnO_6, (f) Sb_3FeO_6, (g) Sb_3NiO_6 and (h) Sb_3CoO_6.

material. For Sb_3TiO_6–NH_3, the computed HOMO and LUMO energies are −7.74 and −3.37 eV, respectively, as shown in Fig. 19(b). The contributions of Sb, Ti, and O to the HOMO are 48.3, 1.30, and 46.01%, respectively. The LUMO is composed of 95.85% Ti. The calculated η, S, μ, ΔE, and ω values for the Sb_3TiO_6 are 2.18 eV, 0.45 eV^{-1}, −5.64 eV, 0.45 eV, and 7.30 eV, respectively. Since the hardness value is larger than 2 eV, the CH_4-adsorbed Sb_3TiO_6 cluster has been identified as a hard material. The calculated HOMO and LUMO energies for Sb_3VO_6–CH_4 are −5.13 and −1.99 eV, respectively, as shown in Fig. 19(c). The HOMO has a 92.19% contribution from V and 6.45% from Sb. The LUMO has 10% contribution from V and 24.09% from Sb. The calculated η, S, μ, ΔE, and ω values for the Sb_3VO_6 cluster are 1.57 eV, 0.63 eV^{-1}, −3.56 eV, 0.63 eV, and 4.04 eV, respectively. The hardness value is less than 2 eV, which indicates that the NH_3-adsorbed Sb_3VO_6 cluster is a soft material. For the Sb_3CrO_6–CH_4 system, the computed HOMO and LUMO energies are −5.85 and −4.22 eV, respectively, as shown in Fig. 19(d). The contributions of Cr and O to the HOMO are 82.57 and 4.20%, respectively. The LUMO is composed of 9.04% Sb, 75.25% Cr, and O 9.22%. The calculated values of η, S, μ, ΔE, and ω for the Sb_3CrO_6 cluster are 0.81 eV, 1.23 eV^{-1}, −5.03 eV, 1.23 eV, and 15.55 eV, respectively. Since the hardness value is less than 2 eV, the CH_4-adsorbed Sb_3CrO_6 has been identified as a soft material. The calculated HOMO and LUMO energies for Sb_3MnO_6–NH_3 are −5.97 and −2.60 eV, respectively, as shown in Fig. 19(e). The HOMO contributions from Sb, Mn, and O are 2.40, 65.10, and 20.50%, respectively. The LUMO contains 80.92% contribution from Mn, 18% from Sb and 5.32% from O. The values of η, S, μ, ΔE, and ω calculated for the Sb_3CrO_6 cluster are 1.68 eV, 0.59 eV^{-1}, −4.28 eV, 0.59 eV, and −5.22 eV, respectively. The hardness value is less than 2 eV, which indicates that the CH_4-adsorbed Sb_3MnO_6 cluster is a soft material.

For the Sb_3FeO_6–CH_4 system, the computed HOMO and LUMO energies are −6.34 and −5.15 eV, respectively, as shown in Fig. 19(f). The contributions of Sb, Fe, and O to the HOMO are 1.40, 50.49, and 29.03%, respectively. The LUMO is composed of 7.07% Sb and 40.61% oxygen. The calculated values of η, S, μ, ΔE, and ω for the Sb_3FeO_6 are 0.59 eV, 1.68 eV^{-1}, −5.74 eV, 1.68 eV, and 27.73 eV, respectively. Since the hardness value is less than 2 eV, the CH_4-adsorbed Sb_3FeO_6 has been identified as a soft material. The calculated HOMO and LUMO energies for the CH_4-adsorbed Sb_3NiO_6 are −6.71 and −2.61 eV, respectively, as shown in Fig. 19(g). The HOMO contributions from Ni, Sb, and O are 3.86, 10.68, and 72.89%, respectively. The LUMO contains 7.4% contribution from Ni, 61.4% from Sb, and 12.36% from O. The Sb_3NiO_6 exhibited η, S, μ, ΔE, and ω values of 2.05 eV, 0.49 eV^{-1}, −4.66 eV, 0.49 eV, and 5.30 eV, respectively. The hardness value was greater than 2 eV, which indicated that CH_4-adsorbed Sb_3NiO_6 is a hard material. For Sb_3CoO_6–NH_3, the computed HOMO and LUMO energies are −7.05 and −3.13 eV, respectively, as shown in Fig. 19(h). The contributions of Sb, Co, and O to the HOMO are 8.30, 41.60, and 43.40%, respectively. The LUMO is composed of 64.05% Co, 4.35% Sb and 20.17% O. The calculated η, S, μ, ΔE, and ω values for the Sb_3CoO_6 are 1.96 eV, 0.51 eV^{-1}, −5.09 eV, 0.51 eV and −5.09 eV, respectively. Since the hardness value is less than 2 eV, the NH_3-adsorbed Sb_3CoO_6 has been identified as a soft material.

3.21. Charge transfer integral (CTI) of the CH_4-absorbed clusters

As discussed above, for Sb_3ScO_6, the CTI-calculated electron- and hole-transfer energies are 0.35 and 0.06 eV, respectively, and the recombination energy from fragment 1 to fragment 2 is 0.49 eV, while the recombination energy from fragment 2 to 1 is 0.04 eV. For Sb_3CrO_6, the calculated electron- and hole-transfer energies are 0.22 and 1.64 eV, respectively, and the recombination energy from fragment 1 to fragment 2 is 0.78 eV, while the recombination energy from fragment 2 to 1 is 0.22 eV. For

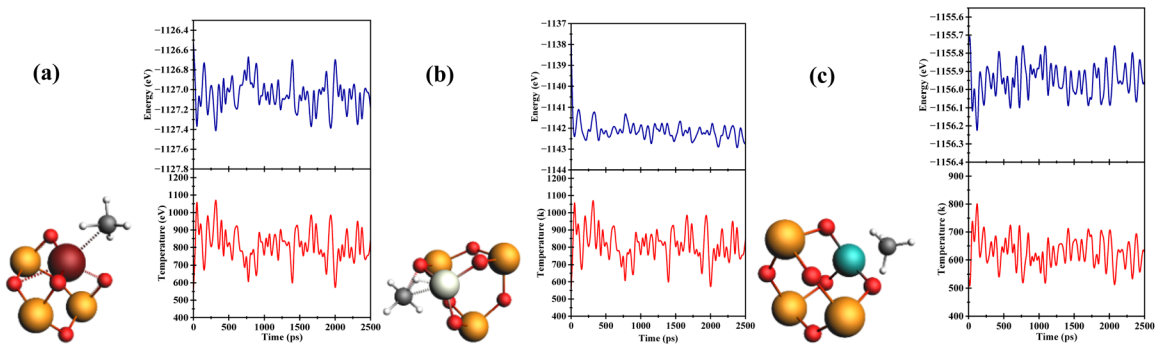

Fig. 21 AIMD simulations of the fully loaded NH_3-absorbed (a) Sb_3ScO_6, (b) Sb_3CrO_6, and (c) Sb_3MnO_6.

Sb_3CrO_6, the calculated electron- and hole-transfer energies are 0.28 and 0.32 eV, respectively, and the recombination energy from fragment 1 to fragment 2 is 0.35 eV, while the recombination energy from fragment 2 to 1 is 0.61 eV. For Sb_3MnO_6, the calculated electron- and hole-transfer energies are 0.05 and 0.08 eV, respectively, and the recombination energy from fragment 1 to fragment 2 is 0.50 eV, while the recombination energy from fragment 2 to 1 is 0.01 eV, as shown in Fig. 20(a)–(h).

3.22. Stability of the fully loaded structure of CH_4-absorbed Sb_3TMO_6

The stability of the SO_2-absorbed Sb_3ScO_6, Sb_3CrO_6, and Sb_3MnO_6 is represented in Fig. 21, which gives snapshots of post-absorption cases and the change in energy and temperature over the time interval.

The AIMD snapshots of the structures and the plots of temperature and energy against time are illustrated in Fig. 21. The energy of all systems remained rather constant over the simulations, as shown in Fig. 21(a), (b) and (c), respectively. The analysis of the structures shows that there is no bond breakage, which indicates the stability of the materials.

3.23. Recovery time (τ)

A crucial factor for determining a gas-sensing material's practical applicability is its recovery time (τ), which establishes the rate at which the sensor is capable of returning to its initial condition following gas desorption. The desorption kinetics of various gases and TMs substituted in the clusters can potentially be quantitatively compared using this method. The findings show that gases with weak-to-moderate adsorption energies, such as CO_2 and NH_3, have short-to-moderate recovery durations, confirming a sensing mechanism dominated by reversible physisorption. For real-time monitoring applications, where rapid sensor replacement is essential, such behavior is ideal.

The computed recovery times for $Sb_3(TM)O_4$ interacting with SO_2, CO_2, NH_3, and CH_4 demonstrate an evident distinction between major and minor desorption modes, which are mainly controlled by the intensity of the gas–surface interactions. Because of its strong chemisorption behavior and high adsorption energies, SO_2 consistently shows the longest recovery times among all TM-doped systems. This indicates the slow desorption kinetics and that external stimuli, including mild heating or UV irradiation, may be necessary for complete sensor regeneration. CO_2, NH_3, and CH_4, on the other hand, show noticeably shorter recovery durations, which are in line with the weak-to-moderate physisorption and enable quick and reversible sensing, making them appropriate for real-time monitoring applications. Although delayed SO_2 desorption indicates strong binding and provides application-dependent selectivity, the overall recovery time trends indicate that $Sb_3(TM)O_4$ is highly generalizable and effective for CO_2, NH_3 and CH_4 detection. A summary of the recovery times for all the gases is represented in Tables S3–S6.

4. Summary

The inorganic molecular clusters belong to a unique class of material employed for diverse applications. This investigation explores the structural and electronic properties of $Sb_3(TM)O_6$ (where TM is Sc, Ti, V, Cr, Mn, Fe, Ni, and Co) using first principles calculations. The TM-dependent adsorption behaviors of CO_2, SO_2, NH_3, and CH_4 indicate whether the TM sites favor stronger or weaker interactions with certain gas molecules. In particular, sensors that incorporate these particular TM sites are predicted to show improved selectivity and sensitivity towards SO_2 under controlled settings due to the significant adsorption energies anticipated for SO_2 on Sb_3TiO_4 and Sb_3VO_4, compared to the weaker interactions for CO_2 or CH_4 on the same clusters. By generating TM-substituted molecular clusters or thin films and monitoring variations in their resistance, current or capacitance in the presence of various gas molecules, this prediction may be verified experimentally. A dual-mode adsorption process is identified by the investigation, with chemisorption taking place for strongly interacting gases and physisorption dominating for weakly interacting gases. In order to verify the anticipated sensing mechanisms, dynamic gas exposure tests were conducted to evaluate visible variations in response time, recovery time, and reversibility.

The thermal stability of all eight pure materials was computed at a temperature of 1000 K. The adsorption energies of the CO_2, SO_2, NH_3, and CH_4 toxic gas molecules on the host zero-dimensional molecular clusters (Sb_3ScO_6, Sb_3TiO_6,

Sb_3VO_6, Sb_3CrO_6, Sb_3MnO_6, Sb_3FeO_6, Sb_3NiO_6, and Sb_3CoO_6) were computed. The electronic properties of all loaded structures were calculated. The stability of the fully loaded configuration for all molecular clusters was computed by AIMD simulations at a temperature of 600 K. QTAIM revealed that the clusters contain strong covalent interactions, while the interaction between the gas molecule and the molecular material is weak. Charge analysis was performed using the charge-transfer integral, which revealed the electronic coupling for both electrons and holes. The anticipated charge transfer and electronic coupling demonstrated different tendencies for electron and hole transport during gas adsorption. In order to validate the recommendations for the $Sb_3(TM)O_6$ sensor materials, these results collectively offer a coherent set of experimentally testable parameters, such as TM-dependent selectivity, adsorption-mode-specific reversibility, structural and electronic perturbations and charge-transport behavior.

Conflicts of interest

The authors declare that they have no known competing financial interests or personal relationships that could have appeared to influence the work reported in this paper.

Data availability

The code for the Amsterdam Density Functional (ADF) can be found at https://www.scm.com. The version of the code employed for this study is 2022.105.[65]

Supplementary information (SI) is available. See DOI: https://doi.org/10.1039/d5ra08222f.

Acknowledgements

The authors extend their appreciation to King Saud University, Saudi Arabia for funding this work through Ongoing Research Funding Program, (ORF-2026-399), King Saud University, Riyadh, Saudi Arabia.

References

1 World Health Organization, *WHO Air Quality Guidelines Global Update 2005: Report on a Working Group Meeting, Bonn, Germany, 18–20 October 2005*, World Health Organization Regional Office for Europe, 2005.
2 N. Z. Raza, *et al.*, First principles study on interactions in inorganic molecular crystals at zero dimensions, *J. Mol. Struct.*, 2024, **1317**, 139102.
3 M. Zhen, Y. Wang, C. Xu, Y. Yi, J. Huang, L. Li and T. You, Dual-enhanced electrochemiluminescence of Au nanoclusters: Ag doping-induced emission and Ce-MOFs-induced excitation, *Biosens. Bioelectron.*, 2025, 117833.
4 A. Majid, *et al.*, Electronic Transport Properties of Molecular Clusters Sb4O6, P4Se3, and P4O6, *J. Phys. Chem. A*, 2024, 4814–4822.
5 T. Ahmad and D. Zhang, A critical review of comparative global historical energy consumption and future demand: The story told so far, *Energy Rep.*, 2020, **6**, 1973–1991.
6 I. Khan, *et al.*, Does energy trilemma a driver of economic growth? The roles of energy use, population growth, and financial development, *Renewable Sustainable Energy Rev.*, 2021, **146**, 111157.
7 B. J. Van Ruijven, E. De Cian and I. Sue Wing, Amplification of future energy demand growth due to climate change, *Nat. Commun.*, 2019, **10**(1), 2762.
8 M. Singla and N. Jaggi, Theoretical investigations of hydrogen gas sensing and storage capacity of graphene-based materials: A review, *Sens. Actuators, A*, 2021, **332**, 113118.
9 H. Cruz-Martínez, *et al.*, Recent developments in graphene-based toxic gas sensors: a theoretical overview, *Sensors*, 2021, **21**(6), 1992.
10 I. Manisalidis, *et al.*, Environmental and health impacts of air pollution: a review, *Front. Public Health*, 2020, **8**, 14.
11 S. Dmitriev, *et al.*, Flexible substrate based gas sensors for air pollution monitoring, *MRS Online Proc. Libr.*, 2004, **814**, I7.14.
12 W. Tsujita, *et al.*, Gas sensor network for air-pollution monitoring, *Sens. Actuators, B*, 2005, **110**(2), 304–311.
13 J. A. Bernstein, *et al.*, Health effects of air pollution, *J. Allergy Clin. Immunol.*, 2004, **114**(5), 1116–1123.
14 A. Raza, *et al.*, Room temperature NH3 gas sensor based on PMMA/RGO/ZnO nanocomposite films fabricated by in-situ solution polymerization, *Ceram. Int.*, 2023, **49**(16), 27050–27059.
15 X. Chen, S. Lv, Y. Liu, H. Gu, X. Sun, Q. Hu and L. Guo, Antiferroelectric SnO2 network with amorphous surface for electrochemical N2 fixation, *Angew. Chem., Int. Ed.*, 2025, **64**(43), e202515222.
16 K. L. Ebi, *et al.*, Extreme weather and climate change: population health and health system implications, *Annu. Rev. Public Health*, 2021, **42**(1), 293–315.
17 H. M. Tran, *et al.*, The impact of air pollution on respiratory diseases in an era of climate change: A review of the current evidence, *Sci. Total Environ.*, 2023, 166340.
18 P. Guo, R. Xue, Q. Zou, X. Ma, C. Su, Z. Zeng and L. Li, Enhanced Ultramicropore of Biomass-Derived Porous Carbon for Efficient and Low-Energy CO 2 Capture: Integration of Adsorption and Solar Desorption, *Energy Environ. Mater.*, 2025, e70140.
19 M. I. Khan, *et al.*, DFT perspective of gas sensing properties of Fe-decorated monolayer antimonene, *Appl. Surf. Sci.*, 2023, **616**, 156520.
20 T. Zhou and T. Zhang, Recent progress of nanostructured sensing materials from 0D to 3D: overview of structure–property-application relationship for gas sensors, *Small Methods*, 2021, **5**(9), 2100515.
21 F. Yan, H. Chen, T. Chi, J. Lu, X. Shen, F. Xie and Z. Zhang, Highly efficient and regenerable amine-impregnated adsorbents: Mechanistic insights into glycerol modification for enhanced direct air capture, *Chem. Eng. J.*, 2025, 166450.

22 M. T. Robinson, *et al.*, Humidity-Initiated Gas Sensors for Volatile Organic Compounds Sensing, *Adv. Funct. Mater.*, 2021, **31**(22), 2101310.
23 M. A. A. Mamun and M. R. Yuce, Recent progress in nanomaterial enabled chemical sensors for wearable environmental monitoring applications, *Adv. Funct. Mater.*, 2020, **30**(51), 2005703.
24 Z. Mohammadi and S. M. Jafari, Detection of food spoilage and adulteration by novel nanomaterial-based sensors, *Adv. Colloid Interface Sci.*, 2020, **286**, 102297.
25 J. Lin, M. Kilani and G. Mao, Recent advances in integrating 1D nanomaterials into chemiresistive gas sensor devices, *Adv. Mater. Technol.*, 2023, **8**(12), 2202038.
26 X. Huang, *et al.*, 25th Anniversary article: hybrid nanostructures based on two-dimensional nanomaterials, *Adv. Mater.*, 2014, **26**(14), 2185–2204.
27 S. Zhu, *et al.*, Research progress of nanomaterials at home and abroad, structure, I. Specific effect and properties of nanomaterials, *Journal of Thermal Processing Technology*, 2010, **31**, 1–5.
28 N. Al-Harbi and N. K. Abd-Elrahman, Physical methods for preparation of nanomaterials, their characterization and applications: a review, *Journal of Umm Al-Qura University for Applied Sciences*, 2024, 1–22.
29 F. Wu and W. P. Hu, Nano materials used in industrial design, *Adv. Mater. Res.*, 2012, **415**, 545–548.
30 L. Ge, *et al.*, Current applications of gas sensor based on 2-D nanomaterial: a mini review, *Front. Chem.*, 2019, **7**, 839.
31 T. Xu, *et al.*, Dual templated synthesis of tri-modal porous SrTiO3/TiO2@ carbon composites with enhanced photocatalytic activity, *Appl. Catal., A*, 2019, **575**, 132–141.
32 X. Qin, H. Cui, L. Guo, X. Li and Q. Zhou, Theoretical Study of Gas Sensing toward Acetone by a Single-Atom Transition Metal (Sc, Ti, V, and Cr)-Doped InP3 Monolayer, *ACS Omega*, 2024, **9**(45), 45059–45067.
33 Y. Cui, *et al.*, Nanowire nanosensors for highly sensitive and selective detection of biological and chemical species, *science*, 2001, **293**(5533), 1289–1292.
34 T. Liu, H. Sun, Y. Zhang, J. Xiao, Y. Lu, C. Niu and Y. Wu, Post-arc electron density measurement in SF6 and SF6/CO2 mixture arcs using Thomson scattering, *Spectrochim. Acta, Part B*, 2025, **229**, 107196.
35 X. Meng, W. Zhuang, L. Lin, H. Li, Z. Cao and H. Mei, Characteristics of streamer discharge in SF6 gas under different pressures, *IEEE Trans. Dielectr. Electr. Insul.*, 2024, 1–99.
36 E. Wongrat, *et al.*, Highly selective room temperature ammonia sensors based on ZnO nanostructures decorated with graphene quantum dots (GQDs), *Sens. Actuators, B*, 2021, **326**, 128983.
37 A. Sutka, *et al.*, Photodoping-Inspired Room-Temperature Gas Sensing by Anatase TiO2 Quantum Dots, *ACS Appl. Nano Mater.*, 2021, **4**(3), 2522–2527.
38 J. H. Lee, *et al.*, Soft-lithographically line-patterned In-doped ZnO quantum dots with hydrothermally grown ZnO nanocolumns for acetone detection, *Sens. Actuators, B*, 2021, **329**, 129131.
39 Z. Shahzamani, *et al.*, Palladium thin films on microfiber filtration paper as flexible substrate and its hydrogen gas sensing mechanism, *Int. J. Hydrogen Energy*, 2019, **44**(31), 17185–17194.
40 S. Matsushima, *et al.*, Electronic interaction between metal additives and tin dioxide in tin dioxide-based gas sensors, *Jpn. J. Appl. Phys.*, 1988, **27**(10R), 1798.
41 T. W. Hesterberg, *et al.*, Critical review of the human data on short-term nitrogen dioxide (NO2) exposures: evidence for NO2 no-effect levels, *Crit. Rev. Toxicol.*, 2009, **39**(9), 743–781.
42 Y. Yong, *et al.*, Ag7Au6 cluster as a potential gas sensor for CO, HCN, and NO detection, *J. Phys. Chem. C*, 2015, **119**(13), 7534–7540.
43 G. Mills, M. S. Gordon and H. Metiu, The adsorption of molecular oxygen on neutral and negative Aun clusters (n= 2–5), *Chem. Phys. Lett.*, 2002, **359**(5–6), 493–499.
44 K. Mondal, A. Banerjee and T. K. Ghanty, Structural and chemical properties of subnanometer-sized bimetallic Au19Pt cluster, *J. Phys. Chem. C*, 2014, **118**(22), 11935–11945.
45 W. Zhang, D. Cheng and J. Zhu, Theoretical study of CO catalytic oxidation on free and defective graphene-supported Au–Pd bimetallic clusters, *RSC Adv.*, 2014, **4**(80), 42554–42561.
46 K. Timsorn and C. Wongchoosuk, Nitrogen-Doped Borophene Quantum Dots: A Novel Sensing Material for the Detection of Hazardous Environmental Gases, *J. Compos. Sci.*, 2024, **8**(10), 397.
47 C. D. Taylor and M. Neurock, Theoretical insights into the structure and reactivity of the aqueous/metal interface, *Curr. Opin. Solid State Mater. Sci.*, 2005, **9**(1–2), 49–65.
48 J. Beheshtian, *et al.*, Computational study of CO and NO adsorption on magnesium oxide nanotubes, *Phys. E*, 2011, **44**(3), 546–549.
49 A. Jamal, M. S. H. Faizi and D. Necmi, Synthesis, structural characterization, DFT calculations, and molecular docking of a novel quinoline derivative, *J. Mol. Struct.*, 2024, **1300**, 137251.
50 A. S. Rad, *et al.*, N-doped graphene as a nanostructure adsorbent for carbon monoxide: DFT calculations, *Mol. Phys.*, 2016, **114**(11), 1756–1762.
51 R. G. Pearson, Chemical hardness and density functional theory, *J. Chem. Sci.*, 2005, **117**, 369–377.
52 R. G. Parr, L. v. Szentpály and S. Liu, Electrophilicity index, *J. Am. Chem. Soc.*, 1999, **121**(9), 1922–1924.
53 O. Prasad, *et al.*, Molecular structure and vibrational study on 2, 3-dihydro-1H-indene and its derivative 1H-indene-1, 3 (2H)-dione by density functional theory calculations, *J. Mol. Struct.:THEOCHEM*, 2010, **940**(1–3), 82–86.
54 B. Kosar and C. Albayrak, Spectroscopic investigations and quantum chemical computational study of (E)-4-methoxy-2-[(p-tolylimino) methyl] phenol, *Spectrochim. Acta, Part A*, 2011, **78**(1), 160–167.
55 N. Yang, Z. Liu and Y. Zhou, CO2 adsorption enhancement and charge transfer characteristics for composite graphene doped with atoms at defect sites, *J. Mol. Model.*, 2023, **29**(2), 60.

56 J. O. L. Fuentes, R. M. del Castillo Vázquez and J. M. Ramirez-de-Arellano, CO2 Absorption on Cu-Doped Graphene, a DFT Study, *Crystals*, 2025, **15**(5), 460.
57 W. Shi, *et al.*, Influence of Cr-and Co-Doped CaO on Adsorption Properties: DFT Study, *Molecules*, 2025, **30**(13), 2820.
58 W. Zhao, *et al.*, Density functional theory study of CO2 adsorption on metal (M= Li, Al, K, Ca) doped MgO, *Mol. Catal.*, 2024, **553**, 113708.
59 S. Wu, *et al.*, Enhancing CO2 Adsorption on MgO: Insights into Dopant Selection and Mechanistic Pathways, *Biomimetics*, 2024, **10**(1), 9.
60 S. Ma, *et al.*, Monolayer Sc2CO2: a promising candidate as a SO2 gas sensor or capturer, *J. Phys. Chem. C*, 2017, **121**(43), 24077–24084.
61 F. Li and H. Asadi, DFT study of the effect of platinum on the H2 gas sensing performance of ZnO nanotube: explaining the experimental observations, *J. Mol. Liq.*, 2020, **309**, 113139.
62 W. Cao, *et al.*, Adsorption and gas-sensing properties of Pt2–GaNNTs for SF6 decomposition products, *Appl. Surf. Sci.*, 2020, **524**, 146570.
63 F.-F. Hu, *et al.*, Nitrogen dioxide gas sensor based on monolayer SnS: A first-principle study, *IEEE Electron Device Lett.*, 2017, **38**(7), 983–986.
64 N. Z. Raza, *et al.*, First principles study on Interaction in Inorganic Molecular Crystals at zero dimensions, *J. Mol. Struct.*, 2024, 139102.
65 G. T. Te Velde, F. M. Bickelhaupt, E. J. Baerends, C. Fonseca Guerra, S. J. van Gisbergen, J. G. Snijders and T. Ziegler, *Amsterdam Density Functional (ADF)*, 2001, https://www.scm.com.